

Integrated thermo-hydraulic heat exchanger modelling for additive manufacturing optimisation

Original

Integrated thermo-hydraulic heat exchanger modelling for additive manufacturing optimisation / Favre, Stefano; Di Blasio, Davide; Fletcher, Tom; Brusa, Eugenio; Delprete, Cristiana. - In: APPLIED THERMAL ENGINEERING. - ISSN 1359-4311. - ELETTRONICO. - 280:(2025). [10.1016/j.applthermaleng.2025.128446]

Availability:

This version is available at: 11583/3003420 since: 2025-09-28T15:07:34Z

Publisher:

Elsevier

Published

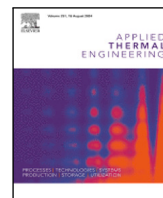
DOI:10.1016/j.applthermaleng.2025.128446

Terms of use:

This article is made available under terms and conditions as specified in the corresponding bibliographic description in the repository

Publisher copyright

(Article begins on next page)



Research Paper

Integrated thermo-hydraulic heat exchanger modelling for additive manufacturing optimisation[☆]

Stefano Favre^a,^{*} Davide Di Blasio^b, Tom Fletcher^b, Eugenio Brusa^a,
Cristiana Delprete^a

^a Politecnico di Torino, Corso Duca degli Abruzzi, 24, Torino, 10129 TO, Italy

^b University of Bath, Claverton Down, Bath, BA2 7AY, United Kingdom

ARTICLE INFO

Keywords:

Heat exchanger
Thermal
Hydraulic
1D model
Additive manufacturing
Fuel cell
Aerospace

ABSTRACT

The design of optimized Heat Exchangers (HE) represents a key asset in the effort towards transport decarbonization and hydrogen-powered electrification due to the low temperatures required for batteries and high amounts of low-grade waste heat produced by fuel cells. At the same time, advancements in the field of Additive Manufacturing (AM) offer new opportunities for unprecedented geometries: enhancing heat transfer, minimising mass and improving compactness. Within this paper, a new methodology is proposed for the modelling of the thermal-hydraulic performance of compact heat exchangers fabricated via AM. Focus is placed towards the realization of a robust and computationally inexpensive tool for evaluating the performance of a wide range of AM heat exchanger geometries for use in multi-objective optimisation. The methodology is based on flexible physics-driven formulations and extensive model parametrization. The proposed approach is verified against experimental data from the literature, exhibiting accurate heat transfer simulation, with a maximum error of 3.7% with respect to the fluids' temperature changes. Initial simulations based on current state-of-the-art models showed significant underestimation of the fluids' pressure drops, of up to -26.4%, when they are applied to AM HEs. However, adjusting the channels' diameter according to the formation of melting droplets, is shown to reduce the maximum hydraulic losses underestimation to just -11.4%. Alternatively, the definition of a calibrated penalty factor, conservatively applied to conventional formulations, allows for the maximum pressure drops to be underestimated by only -4.3%, instead.

1. Introduction

Recent efforts towards the decarbonization of the transport sector require the development of innovative solutions aimed at satisfying current and near future emission targets [1–3]. Powertrain electrification appears as a promising tool for achieving those goals, with numerous initiatives actively investigating and promoting the development of electric propulsion systems in the automotive [4,5], marine [6–9], and aerospace [10,11] technical domains.

A major challenge to current electrification programs is the effective thermal management of state of the art electric energy storage devices, such as batteries [12,13], and electric energy conversion systems, such as fuel cells [14,15]. Typical Li-ion batteries are usually bound to low optimal operating temperatures of about 15 °C to 35 °C [16]. Those values represent a major hindrance to the component's cooling, as the external environment temperature is often very close to the threshold

operating temperature of the battery itself, and may even exceed it. Proton Exchange Membrane (PEM) fuel cells allow for higher operating temperatures of about 60 °C to 80 °C, yet they typically function at reduced efficiencies of approximately 50% [14]. Those conditions lead to significant amounts of low grade waste heat being generated and introduce challenges with providing sufficient component heat dissipation.

The development of suitable cooling systems is therefore crucial for an effective implementation of both batteries and fuel cells [13,17]. However, as a consequence of high power involved with propulsion electrification, providing the required cooling performance is likely to result in cumbersome designs, especially for the system's main radiator. The design, simulation, and optimization of Heat Exchangers (HE) performance thus represent crucial assets in the effort towards carbon footprint reduction and transport electrification. Contemporarily,

[☆] This publication is part of the project PNRR-NGEU which has received funding from the Italian Ministry of University and Research (MUR) - DM352/2022 (CUP n° E12B22000560006)

^{*} Corresponding author.

E-mail address: stefano.favre@polito.it (S. Favre).

<https://doi.org/10.1016/j.applthermaleng.2025.128446>

Received 6 May 2025; Received in revised form 18 September 2025; Accepted 19 September 2025

Available online 25 September 2025

1359-4311/© 2025 The Authors. Published by Elsevier Ltd. This is an open access article under the CC BY license (<http://creativecommons.org/licenses/by/4.0/>).

Nomenclature

A	surface area
a	dimensionless hot fluid parameter, Eq. (4)
a_{Nu}	Nusselt term a for in development laminar flow, Table 2
B	base length (rectangular/square/cuboid shapes)
b	dimensionless cold fluid parameter, Eq. (4)
b_{Nu}	Nusselt term b for in development laminar flow, Table 2
c_p	specific heat at const. pressure
D	diameter (circular/cylindrical shapes)
D_{hyd}	hydraulic diameter (of channels)
f	Nusselt factor f for turbulent and transitional flow, Table 2
f_D	Darcy–Weisbach friction factor
G	mass flux rate
H	HE height
\bar{h}	average convective heat transfer coefficient
K_{contr}	irreversible contraction loss coefficient
K_{exp}	irreversible expansion loss coefficient
K_L	minor losses loss coefficient (in the manifolds)
K_p	pressure drop penalty factor (corrected formulation)
k	thermal conductivity
L	HE length - cold fluid direction
L_{hyd}	channel's hydraulic length
L_{th}	channel's thermal length
m	mass
\dot{m}	mass flow rate
m_{fin}	dimensionless fin parameter of Eq. (18)
\overline{Nu}	Nusselt number (average)
\overline{Nu}_{lam}	laminar Nusselt term for transitional flow, Table 2
\overline{Nu}_{turb}	turbulent Nusselt term for transitional flow, Table 2
n_{fin}	number of fins per layer (equal to channels per row)
n_{layers}	number of layers (rows of fluid channels)
n_{plt}	number of plate-modules
P	perimeter
Pr	Prandtl number
q	heat transfer rate
R	thermal resistance
Ra	arithmetic mean directional roughness
Re	Reynolds number
Re_{crit}	critical Reynolds number
Re_x	local Reynolds number at a given point x
T	fluid temperature
$T(0,0)$	fluid temperature at the plate origin (inlet)
U	global heat transfer coefficient
u	(fluid) velocity

V	volume
W	HE length - hot fluid direction
W_{fin}	geometrical fin width
x	cold fluid direction coordinate
x'	dimensionless cold fluid flow direction coordinate
y	hot fluid direction coordinate
y'	dimensionless hot fluid direction coordinate
Z_{hyd}	hydrodynamic input length
Z_{th}	thermal input length
Δp_{core}	HE core pressure drop
Δp_{header}	header pressure drop
Δp_{ML}	minor losses (pressure drop)
Δp_{rig}	test rig assembly pressure drop

Greek letters

Δ	generic difference
δ_{bl}	boundary layer thickness
ϵ	equivalent sand–grain roughness
ζ_{con}	total convergence resistance coefficient
ζ_{exp}	total divergence resistance coefficient
η_{fin}	fin efficiency
θ	local dimensionless temperature difference between hot and cold fluids
μ	fluid dynamic viscosity
ρ	fluid density
ρ_s	HE structure density
σ	HE porosity
Φ_1	first term of the Churchill's f_D formulation, Eq. (23)
Φ_2	second term of the Churchill's f_D formulation, Eq. (23)
ϕ	ratio of mean to initial temperature difference

Subscripts and abbreviations

AM	additively manufactured
$base$	base surface (space between two fins)
c	cold
$chan$	channel
$cond$	conductive
$conv$	convective
$corr$	corrected
cs	cross-section (or cross-sectional)
$desing$	design value (may differ from the manufactured one)
$dross$	dross (AM-induced)
eq	equivalent
f	fluid
fin	fin
HE	heat exchanger
h	hot
in	in (or inlet)
out	out (or outlet)

several studies are also investigating opportunities introduced by the Additive Manufacturing (AM) processes for innovative and optimized HE geometries [18–20], potentially synergizing with the needs of the transport sector.

Several modelling approaches are proposed in the literature for heat exchanger design, characterization, and optimization. A bidimensional component discretization, combined with empirical regression of the global heat transfer coefficient U and pressure drops, is employed

<i>plt</i>	plate
<i>s</i>	structure (of the HE)
<i>w</i>	wall
0	upstream manifold section (sensor location)
1'	upstream manifold–header junction section
1	section just upstream the HE inlet (outside channels)
2	section just downstream the HE inlet (inside channels)
3	section just upstream the HE outlet (inside channels)
4	section just downstream the HE outlet (outside channels)
4'	downstream header–manifold junction section
5	downstream manifold section (sensor location)

by Khaled et al. [21] to characterize the thermohydraulic behaviour of an innovative multi-passage HE. Torregosa et al. [22] also rely on experimental data fitting to determine the UA value of compact heat exchanger for an electric vehicle's dual purpose air heater-cooler. However, Ref. [22] opts for the lumped $\epsilon - NTU$ formulation for unmixed cross-flow HEs (Incropera [23]), trading detailed modelling of the local HE temperatures for a simplified solution of the heat transfer problem. A similar approach is also adopted by Ruivo et al. [24] for the characterization of the thermal performance of a finned-tube HE via several calibrated models of the Nusselt numbers of both fluids. However, unlike Khaled et al. [21], the studies of Torregosa [22] and Ruivo [24] both neglect modelling the pressure drops entirely. By converse, Kim et al. [25] employ the $\epsilon - NTU$ correlation to characterize a louvred fin compact heat exchanger, addressing the component's heat transfer coefficient and pressure drops via the Colburn j -factor and Fanning f -factor, respectively. Experimental data fitting is then applied to determine both factors dependence on the Reynolds number, improving accuracy under dry/wet operating conditions.

Ultimately, Khaled et al. [21] declare a maximum relative error of the simulated heat transfer of only 3.76%, while Ruivo et al. [24] claim a maximum relative deviation of just 0.9%, for their best calibrated model. Torregosa et al. [22] register a high maximum relative error of 14%, due to limited accuracy of experimental measurements at lower mass flows, yet they still manage to achieve very accurate results, with an average relative error of only 2.4%. Kim et al. [25] observe generally higher deviations, consequent to the simplified formulation of the Colburn and Fanning factors, leading to a rms error of $\pm 16.9\%$ and $\pm 13.6\%$ when determining the j -factor and f -factor, respectively. These results suggest that data regression offers a valuable tool for precise HE performance characterization, with the work of Scott and Joshi [26] advocating for the use of calibrated models in place of complex CFD simulations. Nonetheless, strong dependence on data regression also causes the formulations to be closely tied to the reference HE, limiting opportunities for the investigation of new geometries.

A number of modelling approaches also exist which characterize the HE performance via physical laws, allowing for the formulations to be decoupled from a specific component and associated to its relevant design parameters instead. For instance, the studies by Pujol et al. [27] and Kleiner et al. [28] provide relevant insights into the development of thermal resistance models for the design of cooling channels in electronic heat sinks. In the work of Rasouli et al. [29], the reference $\epsilon - NTU$ equation [23] is employed to quantify the heat transfer of an innovative micro-fin compact HE to be realized via Additive Manufacturing. The global heat transfer coefficient U is determined

via a thermal resistance model based on physical equations and the channels' shapes and dimensions. Pressure drops are still addressed through experimental data regression, due to geometrical complexity of the device, preventing complete decoupling of the modelling approach from the reference configuration. A FEM structural analysis of the HE, and considerations over AM manufacturing constraints are also addressed in [29]. Da Silva et al. [30] model the thermal performance of an Additively Manufactured heat exchanger via combined NTU method and a channels' thermal resistance framework. Ref. [30] also extend the physical modelling to the characterization of HE pressure drops [31].

Overall, Rasouli et al. [29] obtain an average absolute deviation of 3.3% on the simulated component efficiency, with a maximum registered error of 9.2%. Analogously, da Silva et al. [30] achieve a satisfactory average heat transfer error of 3.3% and maximum error of almost 10%. These results evidence that higher flexibility of physics-driven modelling is offset by a generally reduced accuracy in the correlation results. Notably, significant deviations are observed in Ref. [30] when modelling HE pressure drops, with an average relative error of 17.9% and a maximum register error of 27%. These results evidence issues with accurate simulation of hydraulic losses in AM HE, and are in line with trends outlined in the reviews of Kaur and Singh [19], and Careri et al. [20], concerning challenges of HE modelling for AM.

Lim et al. [32] illustrate the use of $\epsilon - NTU$ formulations and thermal resistance frameworks to support the design optimization of bare-tube heat exchangers. Arie et al. [33] apply this concept to the refinement of a microchannel-manifold heat exchanger fabricated via Additive Manufacturing, achieving appreciable performance improvements. However, similarly to the findings of da Silva et al. [30], the study also highlights challenges in accurately modelling pressure drops in AM components, leading to hydraulic losses underestimations of up to 31%. Alternatively, Nacke, Northcutt, and Mudawar propose an innovative modelling approach for the characterization of a finned micro-channel test-plate for AM [34], eventually expanding the methodology to the simulation of a complete HE composed by several layers of these reference modules [35]. The study computes the plate heat transfer by applying differential equations to an infinitesimal, bidimensional discretization of the element. Subsequently, it integrates the differential contributions into a unified sum equation, simplifying the numerical solution. The global heat transfer coefficient U is determined through a thermal resistance model of the plate, whereas pressure drops are disregarded entirely. An average error of approximately 3% is achieved for the calculated heat transfer, while a maximum absolute deviation of 15% is observed at lower mass flow rates, similarly to the findings of Torregosa et al. [22]. The work of Zhuang et al. [36] demonstrates the use of globalized plate models and thermal resistance frameworks in the design optimization of heat exchangers, specifically for an innovative rhombus-fractal heat sink design. The textbook by Nellis and Klein [37] provides in-depth explanations of more traditional methods for solving discretized plates, involving surface meshing to capture local heat exchanger properties and performance. Similar approaches offer enhanced model flexibility and detail, but significantly increase the computational cost of simulations as they require computing the behaviour of each mesh node.

Building on these discretized approaches, Petrovic et al. [38] employ full Computational (Thermo-)Fluid Dynamic (CFD) analyses for the simulation of an additively manufactured heat exchanger featuring complex geometries. The study addresses the component's heat transfer and pressure drops, with satisfactory agreement between predicted and experimental Colburn j -factors, with deviations ranging from 5% to 15%. However, pressure drop predictions are less consistent, underestimating the numerical Fanning f -factors by 11%–32%. Hataway et al. [39] adopt a similar approach, focusing on the integration of self-sustaining geometries for fabrication via AM. However, challenges emerge in achieving consistency with experimental data, resulting in

Table 1
Significant thermal modelling approaches and relevant features for employment in a design optimization loop.

Methodology	Level of detail	Accuracy	Flexibility	Computational efficiency
ϵ -NTU formulation & empirical regression of: • UA [22] • Nusselt equation [24] • Colburn j factor [25]	Global	• High – avg. deviation: 2.5% • Very high – max. deviation: 0.9% • Low – rms error: $\pm 16.9\%$	Very low – limited by fixed ϵ -NTU correlation and empirical model calibration	Very high – no discretization nor iteration (once fitted)
Bidimensional component discretization & empirical regression of U [21]	Local	High – max. deviation: $\approx 3.7\%$	Low – limited by empirical regression of the heat transfer model	Medium-low – reduced by spatial discretization
ϵ -NTU formulation & physical thermal resistance network [29,30]	Global	Medium – avg. deviation: 3.3%, max. $\approx 10\%$	Medium – limited to the adopted ϵ -NTU correlation and resistance model	Medium-high – no discretization, can involve iterative solving
Condensed discretized model & physical thermal resistance network [34,35]	Global	Medium-low – avg. deviation: 3%, max. $\approx 15\%$	High – limited to the adopted thermal resistance model	Medium – no discretization, but includes iterative solving
CFD analyses [38,39]	Local	Medium-low – 5%–15% j -factor deviation [38]	Very high – capable of describing arbitrary geometries and physics	Very low – requires fine discretization, and extensive iteration

a 27% maximum heat transfer overestimation, and a 300% pressure drop underestimation. The study observes that powder residues inside the pipes are the cause of significant discrepancies between numerical simulations and measurements. These results further corroborate the challenges evidenced by Kaur [19], and Careri et al. [20] concerning the effective modelling of AM HE performance, especially with respect to more complex geometries.

CFD analyses offer unmatched simulation versatility but are hindered by significant computational costs, limiting their viability for use in iterative optimization. Consequently, while the use of CFD to support design optimization is common in the literature, it is often limited to the refinement of just one or few key feature parameters [40,41], rarely addressing whole component performance. More extensive optimization strategies involve embedding CFD simulations within topology optimization loops, but these are usually limited to very small control domains due to prohibitive computational requirements. Feppon et al. [42] provide relevant insights into advancements and challenges in the topology optimization of heat exchangers. Recent studies focus on leveraging periodic repetitions in the geometry and cellular designs to reduce the computational costs of these methodologies [43,44].

Alternatively, Beltrame et al. [45] and Mophatra et al. [46] propose using surrogate models to support fast design optimization of heat exchangers. These reduced-order models significantly improve computational efficiency, but require extensive training on pre-existing databases of optimized designs. Additionally, their range of applicability remains limited to the geometries included in the training set. However, recent efforts propose training of Artificial Neural Networks over CFD simulation as a promising approach for defining improved surrogate models [47,48].

The literature provides several modelling approaches for the performance evaluation of heat exchangers, each presenting different trade-offs between accuracy, versatility, and computational efficiency, as illustrated in Table 1. Nonetheless, a growing need for enhanced HE design optimization demands for the development of new, flexible, and robust simulation tools, presenting strong correlation with the geometrical parameters, reliable thermal and hydraulic performance prediction, and reduced computational costs. Additionally, numerous publications highlight that challenges remain with the accurate modelling heat exchanger fabricated via Additive Manufacturing, particularly for pressure drops' prediction.

This paper aims to address these gaps, presenting a renewed, comprehensive modelling approach for the analysis of cross-flow heat exchangers featuring rectangular and circular shaped ducts. This configuration is chosen due to its widespread adoption in transport sector cooling, particularly with radiators, and serves as a suitable benchmark for this study. The methodology integrates the versatile and efficient thermal framework developed by Nacke et al. [34,35], with the hydraulic model adopted by da Silva et al. [30], for a complete characterization of the component.

Key features of the presented approach are: a strong correlation of the governing equations with the physics and geometry of the HE, a high model adaptability to different shapes and dimensions, and a generally low computational cost. The numerical implementation is also addressed carefully, aiming to minimize the required simulation inputs, improve numerical robustness, facilitate tool up-gradability, and ultimately favour future integration into a design optimization framework. These features are essential to ensure that the methodology is generalized and readily available for use in the broader effort towards transport decarbonization and emission mitigation. In particular, this study aims to provide an innovative tool for the rapid performance assessment of compact heat exchangers, serving as the fundamental element to support new design optimization frameworks for the rapid conceptualization of enhanced HE.

Finally, a physics-driven corrective formulation and a regression-driven adjusted equation are proposed to account for inconsistencies in pressure drop simulation for AM HE. Robustness of the approach is ultimately tested and validated against experimental data from the literature, allowing for a preliminary verification of the model's accuracy.

2. Methodology

The proposed methodology addresses three main aspects of HE performance characterization. First the component's thermal behaviour is analysed and discussed to model the heat exchanger's outlet temperatures and transferred heat. Second, the hydraulic performance of the heat exchanger is introduced and modelled, simulating the pressure drop across the components. Finally, the volumetric and gravimetric parameters are evaluated, providing details on the masses and volumes associated with the thermal fluids and the enclosing structure.

2.1. Theoretical thermal model

When modelling the thermal performance of a compact heat exchanger, symmetries in the design can be exploited to virtually divide the component into several geometrically identical stacked elements, each exhibiting comparable thermal behaviour [35]. This approach simplifies the characterization of the device reducing the component's analysis to the simulation of a single fundamental module. Negligible differences can then be assumed in the temperature distribution along the stacking direction of the modules, allowing for the plates' description to be further simplified from a tridimensional formulation to a bidimensional one. The thermal performance of the entire heat exchanger is then obtained by replicating and combining the behaviour of a single 2D plate across all stacked elements of the component. This concept is illustrated in Fig. 1.

The following hypotheses are applied for the development of the HE thermal model:

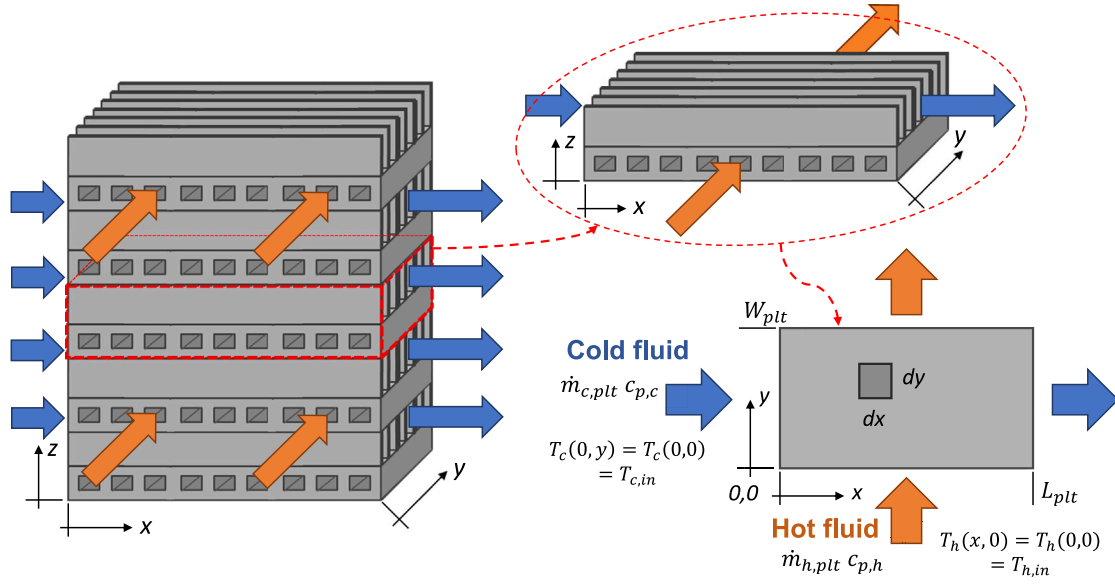


Fig. 1. Representation of the whole heat exchanger component and detail of a single plate module with the associated bidimensional system of coordinates.

- **Steady state model.**
- **Uniform flow distribution** across all plates and all channels within a plate.
- **Uniform global heat transfer coefficient (U)** across the plate, which is equivalent to the average value of all local heat transfer coefficients of the module.
- **Uniform and constant fluid properties**, equivalent to the mean value between the average inlet and outlet fluid properties.
- **Negligible heat loss** of the heat exchanger with respect to the external environment.
- **Negligible axial conduction**, which leads to the heat transfer only occurring perpendicularly to both fluids' flow directions.
- **Adiabatic fin tips.** In the thermal resistance framework of a single plate-module, the channels' walls behave as fins, with the channels' centreline identifying the fin tips. The fin tips thus define a symmetric boundary with respect to the fins of the adjacent module, which are under identical conditions, leading to no heat transfer occurring through the tips, as illustrated in Fig. 2.

2.1.1. Heat transfer equations and outlet temperatures

In line with that set of hypotheses, a single heat exchanger layer, in the form of a plate module, is effectively described through a bidimensional system of coordinates, parallel to both fluids flows, as shown in Fig. 1. Differential equations modelling the heat transfer rate perpendicular to this system of coordinates are then applied to a generic infinitesimal element of the plate, resulting in three distinct formulations. These include: an equation describing the heat transfer crossing the infinitesimal element surface, Eq. (1), and two equations expressing the heat exchange as perceived from both fluids, the hot one, Eq. (2) and the cold one, Eq. (3), as it drives their change in temperature.

$$dq = U(T_h - T_c)dxdy \quad (1)$$

$$dq = -\frac{\dot{m}_{h,plt}}{L_{plt}}c_{p,h}\frac{\partial T_h}{\partial y}dxdy \quad (2)$$

$$dq = +\frac{\dot{m}_{c,plt}}{W_{plt}}c_{p,c}\frac{\partial T_c}{\partial x}dxdy \quad (3)$$

Those three equations can then be combined, differentiated, and refined via the use of Laplace transforms, allowing for the definition of a

dimensionless temperature difference ratio θ , as proposed by J. L. Mason [49]. Eq. (4) provides this ratio, expressing the dimensionless local temperature difference between hot and cold fluids, normalized by the inlet temperature difference.

$$\theta(x', y') = \frac{T_h - T_c}{T_h(0,0) - T_c(0,0)} = e^{-(ay'+bx')} \cdot \sum_{n=0}^{\infty} \frac{(abx'y')^n}{(n!)^2} \quad (4)$$

Where:

$$a = \frac{U W_{plt} L_{plt}}{\dot{m}_{h,plt} c_{p,h}}, \quad b = \frac{U W_{plt} L_{plt}}{\dot{m}_{c,plt} c_{p,c}}, \quad x' = \frac{x}{L_{plt}}, \quad y' = \frac{y}{W_{plt}}$$

The total heat transfer rate occurring across the plate is evaluated by integrating Eq. (1) over the entire surface of the bidimensional module. The integration limits are normalized with respect to the plate's main dimensions, while the integrand is scaled with respect to the fluids inlet temperature difference, leading to Eq. (5).

$$q_{plt} = [T_h(0,0) - T_c(0,0)] \int_0^1 \int_0^1 U \frac{T_h - T_c}{T_h(0,0) - T_c(0,0)} \times W_{plt} L_{plt} d\left(\frac{x}{L_{plt}}\right) d\left(\frac{y}{W_{plt}}\right) \quad (5)$$

The obtained formulation can then be combined with the θ ratio definition from Eq. (4), allowing for the identification of a ϕ value, representing the ratio of the mean to initial temperature difference, as shown in Eq. (6).

$$\phi = \frac{q_{plt}}{U W_{plt} L_{plt} [T_h(0,0) - T_c(0,0)]} = \int_0^1 \int_0^1 \theta d(x') d(y') \quad (6)$$

The elicitation of the θ value within the integrals of Eq. (6) allows for the formalization of the ϕ expression shown in Eq. (7). This enables to condense the discretized plate model into a single formulation, eliminating the need to characterize a full mesh grid and perform a complete CFD analysis. As a result, detailed mapping of local performance is lost, but computational costs are significantly reduced, while preserving flexibility and ensuring strong correlation with the plate geometry. Details over the mathematical demonstration leading to this formulation are provided within the work of Nacke et al. [34].

$$\phi = \frac{1}{ab} \sum_{n=0}^{\infty} \left[1 - e^{-a} \sum_{k=0}^n \frac{a^k}{k!} \right] \left[1 - e^{-b} \sum_{k=0}^n \frac{b^k}{k!} \right] \quad (7)$$

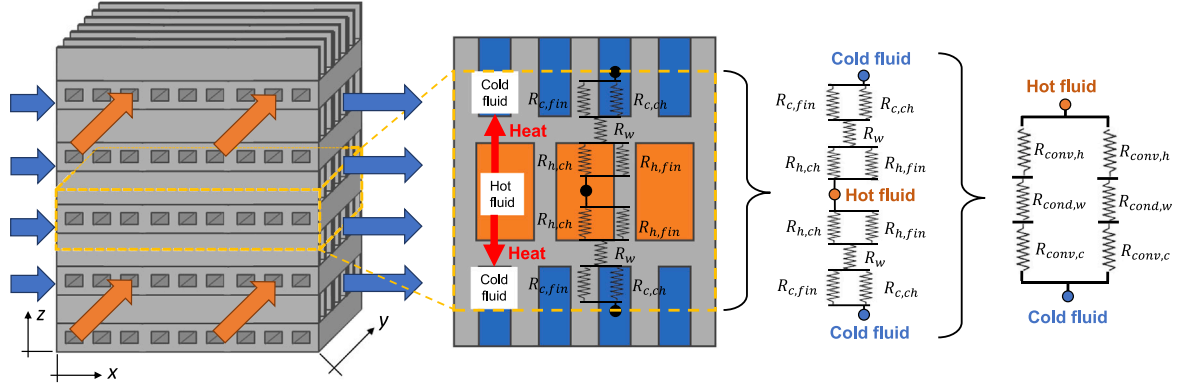


Fig. 2. Representation of the plate control volume centred around the channels of one fluid, and extrapolation of the equivalent thermal resistance model. To ease visualization, the channels of both fluids are shown with cross-sections perpendicular to the reader, although the heat exchanger operates in a cross-flow configuration.

The obtained value of ϕ is thus be employed to solve the plate's heat transfer rate of Eq. (6) by rearranging it into Eq. (8).

$$q_{plt} = U W_{plt} L_{plt} [T_h(0,0) - T_c(0,0)] \phi \quad (8)$$

Similarly, by combining Eq. (8) with Eqs. (2) and (3), it is also possible to determine the average outlet temperatures of the hot and cold fluids, respectively.

$$\bar{T}_{plt,h,out} = T_h(0,0) - a [T_h(0,0) - T_c(0,0)] \phi \quad (9)$$

$$\bar{T}_{plt,c,out} = T_c(0,0) + b [T_h(0,0) - T_c(0,0)] \phi \quad (10)$$

The results of a single plate-module can then be extended to the whole heat exchanger component. Notably, the proposed methodology is developed in Refs. [34,35] to characterize heat exchangers featuring an equal number of channel rows for both fluids. Consequently, in the reference, each layer of hot fluid channels can effectively be paired with an adjacent layer of cold ducts to form a plate, with no remainders.

However, there are also instances where the total number of layers of a given fluid may differ from that of the other. This is exactly the case of the compact heat exchanger examined in Ref. [30], which comprises 9 rows of hot fluid channels, and 10 rows of cold fluid channels. To account for these occurrences, a corrective formulation is herein proposed, assuming any unpaired rows of channels to behave adiabatically with respect to the surrounding layers. Consequently, the total number of plates contributing to the modelling of the heat transfer phenomenon can be assumed to be equal to the number of layers of the fluid with fewer rows, as shown in Eq. (11).

$$n_{plt} = \min(n_{h,layers}, n_{c,layers}) \quad (11)$$

The total heat transfer rate of the heat exchanger is thus defined through the combination of all plates' thermal contributions, as shown in Eq. (12).

$$q_{HE} = q_{plt} * n_{plt} \quad (12)$$

The outlet temperatures of the fluids are defined, instead, as the weighted average of all plates outlet temperatures, according to Eq. (13). Where the outlet temperature of an eventual unpaired layer is simply assumed to be equal to the inlet temperature of that same fluid, consequent to the adiabatic layer hypothesis.

$$\bar{T}_{HE,out} = \frac{\bar{T}_{plt,out} \cdot n_{plt} + \bar{T}_{plt,in} (n_{layers} - n_{plt})}{n_{layers}} \quad \text{Where: } \bar{T}_{in} = T_{0,0} \quad (13)$$

2.1.2. Heat transfer coefficient U and thermal resistances

With the heat transfer equation completely defined, it is now necessary to specify the plate's global heat transfer coefficient U , by the area with respect it is defined A . A thermal resistance scheme is thus employed to determine UA_{plt} while, for the purpose of this study, the reference area A_{plt} is assumed as the product between the two main module's dimensions, W_{plt} and L_{plt} . The heat exchanger's symmetry is hence exploited once again, shifting the plate's control volume to be centred around the channels of just one of the two fluids, while preserving the dimensions and thermal balance of the control domain. This allows for a parallel of two identical thermal resistances to be defined, and the value of UA_{plt} elicited, according to Eq. (14). The two thermal resistance branches are then further decomposed into a series of three thermal resistances describing the hot fluid convection, the separating wall conduction, and the cold fluid convection, as shown in Eq. (15). This whole concept is exemplified in Fig. 2.

$$R_{plt} = \left(\frac{1}{R_{branch}} + \frac{1}{R_{branch}} \right)^{-1} = \frac{R_{branch}}{2} \quad \text{where } R_{plt} = (UA_{plt})^{-1} \quad (14)$$

$$R_{branch} = R_{conv,h} + R_{cond,w} + R_{conv,c} \quad (15)$$

The conductive term of Eq. (15) is determined through Eq. (16).

$$R_{cond,w} = \frac{H_w}{k_s W_{plt} L_{plt}} \quad (16)$$

Where H_w represents the height, and thus the thickness, of the walls separating the two fluids, and k_s is the thermal conductivity of the material composing the heat exchanger.

The fluids' thermal resistances, instead, are further decomposed into two separate terms, one being associated with the heat exchange occurring through the channels' base surface, and the other with the heat transfer occurring along the channels' sidewalls, which effectively act as fins, as shown in Fig. 2. Those two terms effectively act as a resistance parallel, however, thanks to the adiabatic fin tip hypothesis, it is possible to combine them into a single equivalent thermal resistance, here represented in Eq. (17).

$$R_{conv} = \frac{1}{n_{fin}(\eta_{fin} \bar{h}_{fin} A_{fin} + \bar{h}_{base} A_{base})} \quad (17)$$

Where n_{fin} is the number of fins of a given fluid within a plate-module, and is equivalent to the fluid's number of channels per plate. The parameters η_{fin} , \bar{h}_{fin} and A_{fin} represent, respectively, a single half-fin efficiency, its associated average heat transfer coefficient, and its wet area. Finally, \bar{h}_{base} and A_{base} express the average heat transfer coefficient and wet area of a single channel base surface.

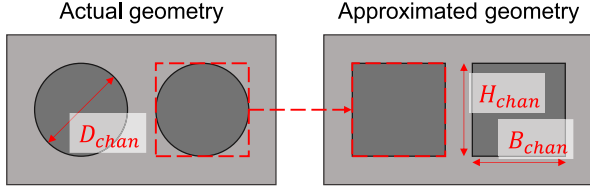


Fig. 3. Circular ducts approximation assumed to simplify fin efficiency calculation.

The fin efficiency formulation for fins with an adiabatic fin tip is presented in Eq. (18), and employed for both fluids.

$$\eta_{fin} = \frac{\tanh\left(m_{fin} \frac{H_{fin}}{2}\right)}{m_{fin} \frac{H_{fin}}{2}} \quad (18)$$

Notably, as anticipated, only half of the geometrical fin height ($H_{fin}/2$) is considered when modelling each branch of the thermal resistance parallel, consequent to the adiabatic fin tip hypothesis at the channels centerline. The m_{fin} factor is defined, instead, via Eq. (19).

$$m_{fin} = \sqrt{\frac{\bar{h}_{fin} P_{fin,cs}}{k_s A_{fin,cs}}} \quad (19)$$

Where $P_{fin,cs} = 2(W_{fin} + L_{fin})$ and $A_{fin,cs} = W_{fin} \cdot L_{fin}$ are the fins' cross sectional perimeter and area, respectively.

Several Nusselt formulations are employed for the characterization of the convective heat transfer coefficients, \bar{h}_{fin} and \bar{h}_{base} , of both fluids [23]. Details of the adopted formulations are provided in Appendix A, along with some considerations over the adequate identification of fluids flow regimes.

Notably, the decoupling of the plate model and ϕ equation from the thermal resistance framework ensures that the two can be independently addressed and updated to represent different configurations. For instance, Ref. [35] demonstrates the high adaptability of Eq. (7) in solving plate heat transfer in both rectangular and annular HE configurations. Ref. [34], instead, distinguishes between mixed-flow and separate-flow heat transfer through slight modifications of the thermal resistance formulation and fin parameters.

Hence, thermal modelling of circular shaped ducts is specifically addressed following Ref. [30], and assumes that a square channel, circumscribing the circular duct, could effectively be employed to simplify solving Eqs. (17) and (18). Consequently, the fin efficiency and convective thermal resistance of circular shaped channels are herein approximated through an equivalent square duct, as illustrated in Fig. 3 and defined according to $D_{chan} = B_{chan} = H_{chan}$.

2.2. Theoretical hydraulic model

When modelling the hydraulic performance of a compact heat exchanger, Shah and Sekulić [31] identified three main sources of pressure drop within the component. These are: the flow contraction at the HE inlet, the friction and thermal expansion (or contraction) along the channels, and the flow expansion at the HE outlet, as illustrated in Fig. 4. Each of these contributions is then further decomposed into an ideal and an irreversible term, which can later be collected into a single formulation, assuming a few additional hypotheses:

- **Uniform velocity profile.**
- **Constant fluid properties.**
- **Incompressible fluid flow**, assuming Mach numbers lower than 0.3 [50]. Since air is the only compressible fluid of interest for this study, this hypothesis can be considered valid as long as the gas speed is not greater than 100 m s^{-1} .

The resulting comprehensive pressure drop formulation for compact heat exchangers is thus provided in Eq. (20) [31], as per Ref. [30].

$$\Delta p_{core} = \Delta p_{14} = \frac{G^2}{2\rho_2} \left[(1 - \sigma^2) + K_{contr} + 2 \left(\frac{\rho_2}{\rho_3} - 1 \right) + \left(f_D \frac{L_{hyd}}{D_{hyd}} \rho_2 \left(\frac{1}{\rho} \right) \right) - \frac{\rho_2}{\rho_3} (1 - \sigma^2) + \frac{\rho_2}{\rho_3} K_{exp} \right] \quad (20)$$

Where the polynomial's first and second terms represent the pressure losses at the HE inlet; the third and fourth terms describe the pressure drops within the channels; and the fifth and sixth terms characterize the pressure change at the component's outlet. σ expresses the heat exchanger's porosity, defined as the ratio between the total cross-sectional area of all channels by the heat exchanger's upstream area. It's value is assumed identical for the inlet and outlet sections and is provided through Eq. (21). G represents the fluid mass flow rate scaled by the total cross-sectional area of all heat exchanger's channels, which are also assumed to be equal $A_{2,cs} = A_{3,cs}$, as indicated in Eq. (22).

$$\sigma = \frac{A_{2,cs}}{A_{1,cs}} = \frac{A_{3,cs}}{A_{4,cs}} \quad (21)$$

$$G = \frac{\dot{m}_{HE}}{A_{2,cs}} = \frac{\dot{m}_{HE}}{A_{3,cs}} \quad (22)$$

The K_{contr} and K_{exp} factors represent two coefficients of irreversibility respectively associated with the contraction, and expansion, of a fluid's flow. These coefficients are derived from empirical diagrams by Kays and London [51], and here parametrized into tabulated data to allow for the factors to be autonomously adjusted by the model accordingly to the simulated geometry. ρ_2 and ρ_3 express the fluid densities at the heat exchanger inlet and outlet, respectively, which, under incompressible flow hypothesis, can also be assumed to be equal to the densities immediately upstream $\rho_1 = \rho_2$ and downstream $\rho_4 = \rho_3$ the HE. L_{hyd} and $D_{hyd} = 4 \cdot A_{chan,cs} / P_{chan,cs}$ define a single channel's length and hydraulic diameter, both assumed to be constant and equal across all component's ducts. $\left(\frac{1}{\rho} \right)$ denotes the average value of a fluid's reciprocal densities across a channel, which can be approximated as $(\bar{\rho})^{-1}$ when density changes are small. Finally, f_D introduces the Darcy friction factor of the channels, defined according to the Churchill's formulation of Eq. (23) [52]. This empirical correlation is preferred over the traditional Darcy–Colebrook equation [23], as it provides an explicit expression of f_D , which spans all flow regimes without discontinuities.

$$\begin{cases} \Phi_1 = \left[-2.457 \ln \left(\left(\frac{7}{Re} \right)^{0.9} + 0.27 \frac{\epsilon}{D_{hyd}} \right) \right]^{16} \\ \Phi_2 = \left[\frac{37530}{Re} \right]^{16} \\ f_D = 8 \left[\left(\frac{8}{Re} \right)^{12} + (\Phi_1 + \Phi_2)^{-1.5} \right]^{\frac{1}{12}} \end{cases} \quad \text{Where } Re = \frac{\rho u D_{hyd}}{\mu} \quad (23)$$

The formulation also accounts for the influence of surface roughness when entering transitional and turbulent flow regimes. Additionally, to account for Reynolds number variations within the channels, the Darcy friction factor is herein evaluated as a function of the fluid's mean velocity \bar{u} , density $\bar{\rho}$ and dynamic viscosity $\bar{\mu}$, each defined as the average value between sections 2 and 3 from Fig. 4. However, direct turbulence initiation criteria, like lowering of the critical Reynolds number Re_{crit} on surfaces featuring pronounced textures, are neglected at the current stage of this work.

ϵ expresses the equivalent Colebrook sand–grain roughness, which does not correspond to a physically measurable surface feature and is therefore not directly accessible. As a first-order estimate, Ra/D_{hyd} is assumed for a preliminary approximation of the ϵ/D_{hyd} ratio, following Refs. [30,53,54]. This assumption leverages the extensive use of the arithmetic mean roughness Ra for experimental measurements in the literature and industry [53], but remains a rough approximation, as Ra fails to fully characterize all surface texture's attributes.

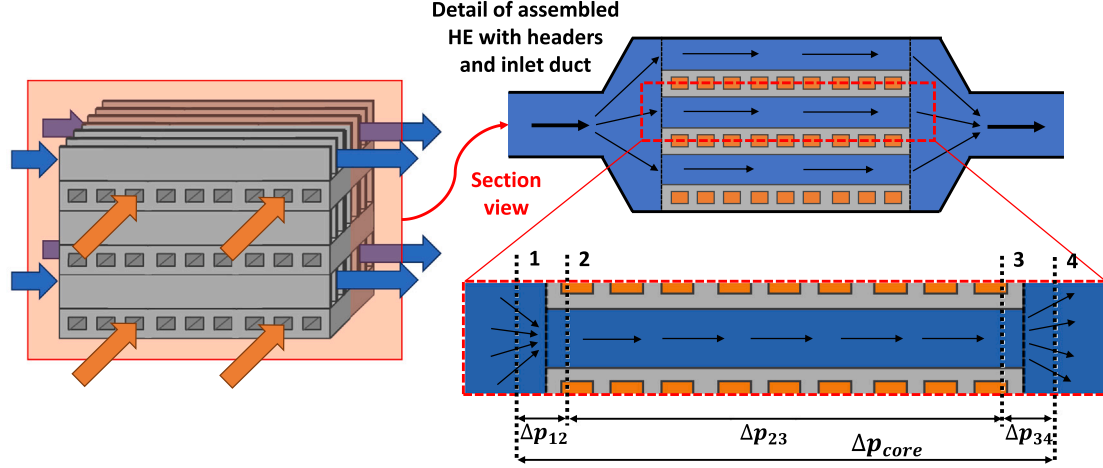


Fig. 4. HE representation and subdivision according to the inlet, mid, and outlet pressure drop contributes proposed by the adopted modelling approach.

2.3. Volumes and masses model

When modelling the gravimetric performance of a compact heat exchanger, the total volume of the radiator is evaluated through Eq. (24), approximating the component as a rectangular cuboid. The volumes filled by the fluids are instead assessed through Eq. (25), for the hot medium, and Eq. (26), for the cold one, assuming the channels as straight prismatic ducts. The base area of the ducts is defined through Eq. $A_{chan,cs} = \pi \frac{D^2}{4}$ for circular channels, and Eq. $A_{chan,cs} = B_{chan} \cdot H_{chan}$ for rectangular ones. Ultimately, the space occupied by the heat exchanger's main structure is obtained by subtracting the fluids' volumes to the total HE volume, as of Eq. (27).

$$V_{HE} = L_{HE} \cdot W_{HE} \cdot H_{HE} \quad (24)$$

$$V_h = (n_{h,layers} \cdot n_{h,fin}) \cdot A_{h,chan,cs} \cdot W_{HE} \quad (25)$$

$$V_c = (n_{c,layers} \cdot n_{c,fin}) \cdot A_{c,chan,cs} \cdot L_{HE} \quad (26)$$

$$V_s = V_{HE} - V_h - V_c \quad (27)$$

Where L_{HE} , W_{HE} , and H_{HE} are the heat exchanger's length, depth, and height, respectively; while the products $n_{h,layers} \cdot n_{h,fin}$ and $n_{c,layers} \cdot n_{c,fin}$ indicate the total number of channels of the two fluids.

The masses associated with the HE fluids and structure are then calculated by multiplying each volume by its relative material density $m = V \cdot \rho$, assuming averaged densities $\bar{\rho} = (\rho_2 + \rho_3)/2$ for the thermal media, and tabulated material proprieties for the structure. Ultimately, the total heat exchanger mass is defined summing the masses of all elements: the fluids, and the structure, according to Eq. (28).

$$m_{HE} = m_h + m_c + m_s = V_h \cdot \rho_h + V_c \cdot \rho_c + V_s \cdot \rho_s \quad (28)$$

3. Numerical implementation and validation

A numerical simulation model is developed to provide fast and automated performance assessment of compact, cross-flow heat exchangers, implementing the thermal, hydraulic, and gravimetric equations previously described in Section 2. High tool modularity is ensured by independently addressing each of these three aspects through a dedicated, fully functional, Python script, allowing for the proposed framework to be easily updated and expanded to the analysis of alternative design and configurations. Finally, a comprehensive characterization of the HE is achieved through a model integration script, tasked with orchestrating the execution of the three base codes, as show in Fig. 5.

The dimensions presented in Fig. 6 are provided as inputs to the model, while the remaining geometrical parameters of interest, such as channels' wet surfaces and hydraulic diameters, are extracted by the tool. The fluid's mass flow rates, inlet temperatures, and outlet pressures are then provided to define a component's operating condition to be simulated. The determination of all relevant fluid properties within the model is handled via the Cool-prop Python library, from Bell et al. [55]. Details concerning the execution and integration of the thermal and hydraulic models are provided in the following sections.

3.1. Numerical thermal model

The numerical thermal model is designed to calculate the outlet temperatures of the fluids, taking the inlet temperatures and both pressures as inputs.

An iterative approach is developed to refine the simulated mean fluid properties, for an accurate determination of the thermal performance in Eq. (17). A negligible heat transfer hypothesis is initially assumed, resulting in the first try expected outlet temperatures being $T_{in} = T_{out}$, i.e. $T_2 = T_3$. The outlet properties are then derived from these temperatures and averaged with the inlet properties to compute the heat transfer and determine the calculated outlet temperatures. These temperatures are then employed to extract a new set of refined outlet properties, and the process is repeated until the computed temperatures converge with the assumed ones, as shown in Fig. 5. A temperature refinement tolerance of 0.01 °C is assumed as the target accuracy threshold for stopping the iteration.

A new iterative approach is also devised to calculate ϕ , leveraging the diminishing influence of higher-order terms in Eq. (7) to approximate the equation's infinite sum as finite, and solve it numerically. The equation is solved with an initial upper summation limit of 1, which is progressively increased to include additional terms and refine ϕ . Iterations stop once the contribution of the added terms falls below 0.01% of the current cumulative sum, or when a maximum of 50 iterations is reached. Notably, all simulations in this study achieved convergence well before reaching the iteration limit, with only two iterations being required, corresponding to the first three terms of the ϕ sum.

3.2. Numerical hydraulic model

The numerical hydraulic model is designed to calculate the pressure drops of both fluids, and the resulting absolute inlet pressures, taking the outlet pressures and both temperatures as inputs.

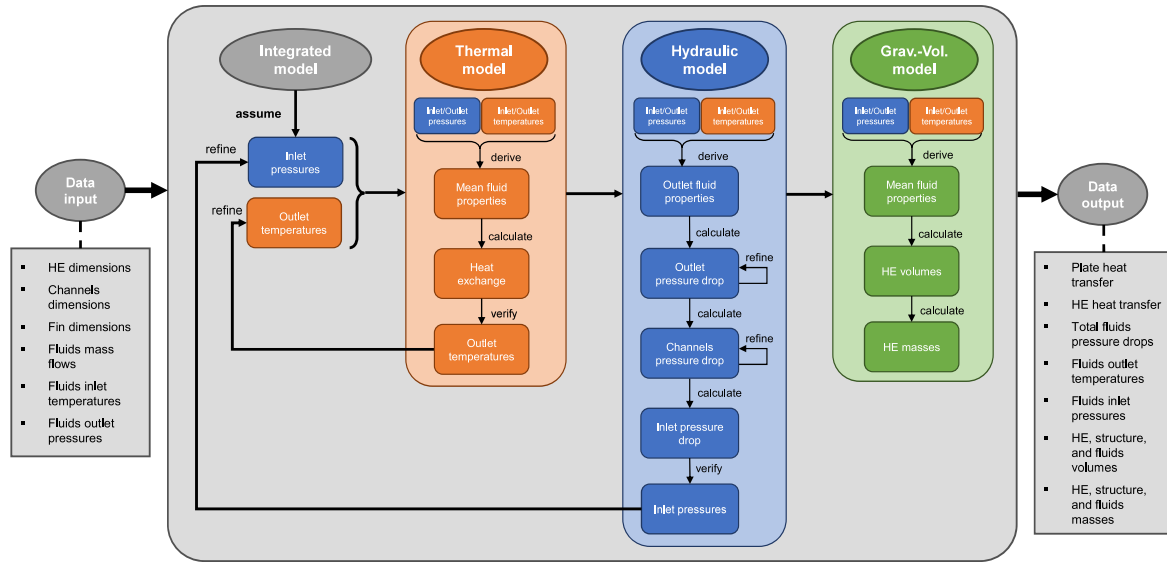


Fig. 5. Functional scheme of the integrated HE characterization model, including detail of the thermal, hydraulic, and gravimetric/volumetric sub-models.

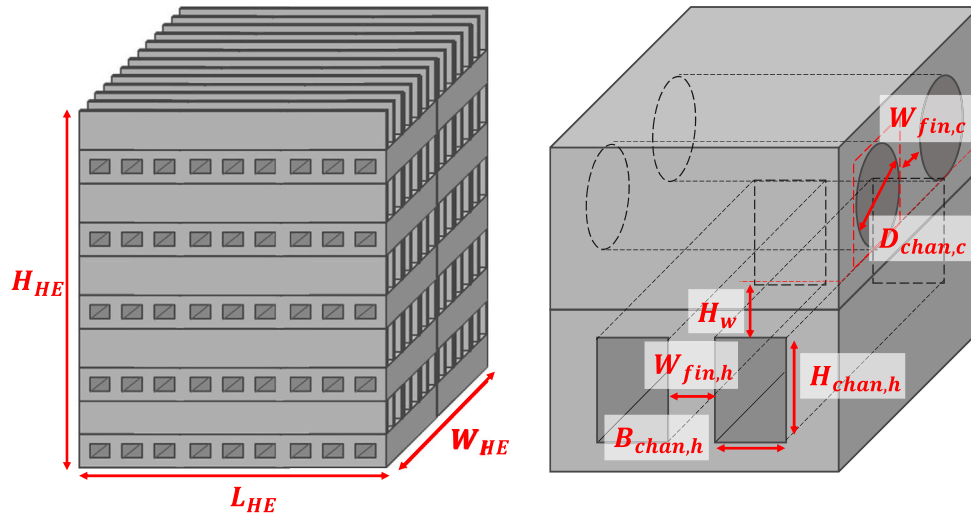


Fig. 6. Representation of all geometrical inputs required by the model. A combined circular-rectangular channel design is provided, on the left, to evidence differences between parameters of the two shapes.

Modelling is performed starting from the HE's outlet section and moves upstream, unlike in the thermal script. The absolute pressures are evaluated step by step for each section by adding the loss terms computed via Eq. (20), as illustrated in Fig. 5. This setup was conceived to minimize the likelihood of simulating negative pressures at any point in the HE, which might occur if the hydraulic losses were to be subtracted instead. Such occurrences would not only result in a non-physical representation of the component, but would also introduce numerical instabilities and errors when accessing fluid databases, ultimately restraining the model from employment in an optimization loop.

Two iterative loops are defined here as well, to refine the local fluid properties of sections 2 and 3 for an accurate estimation of the K_{exp} term from Eq. (20), and the channels' mean properties. A negligible pressure drop is initially assumed for both sections, leading to $p_3 = p_4$ and $p_2 = p_3$. The fluid properties are then extracted based on these pressures and employed to compute the HE losses and the resulting upstream pressures. These pressures are finally employed to derive a new set of refined properties, repeating the process until the simulated pressures match the assumed ones. The loop is first executed until

convergence for Section 3, and subsequently applied to Section 2. A pressure refinement tolerance of 100 Pa is adopted as the target accuracy threshold for terminating the iteration.

3.3. Numerical integrated model

Ultimately, a numerical integration script combines the results of the previously described thermal and hydraulic models with the volumetric and gravimetric formulations from Section 2.3, to provide a more comprehensive characterization of the HE. This modelling methodology only requires the fluids' inlet temperatures and outlet pressures as thermo-hydraulic inputs, and returns the simulated outlet temperatures and inlet pressures.

Effective integration of the thermal and hydraulic models needs to account for the fact that both the inlet pressures and outlet temperatures are unknown a priori. An external loop is thus introduced, iterating between the two models to progressively refine the determination of both parameters. The initial assumptions of negligible heat transfer and pressure drop are extended to the upstream and downstream sections of the HE, leading to first try hypotheses of

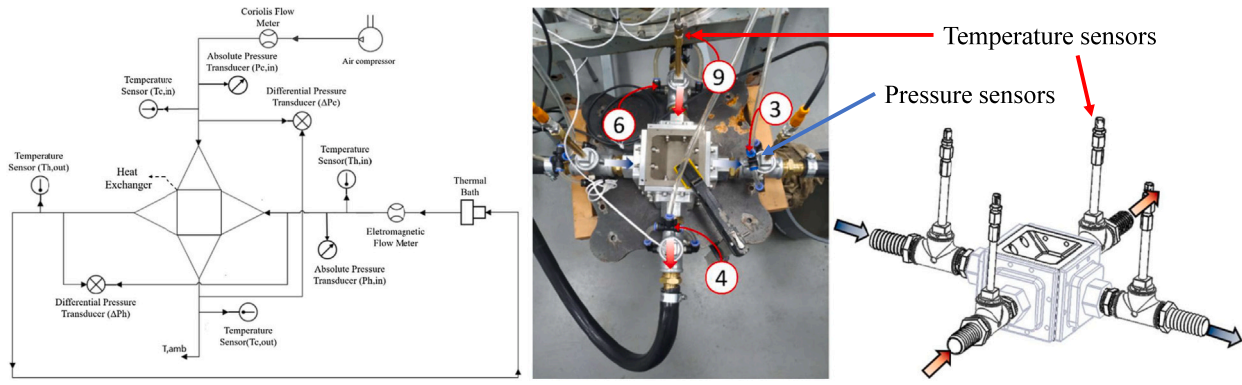


Fig. 7. Test rig from Ref. [30] and detail of sensor placement for the experimental collection of pressure drops and temperature data.

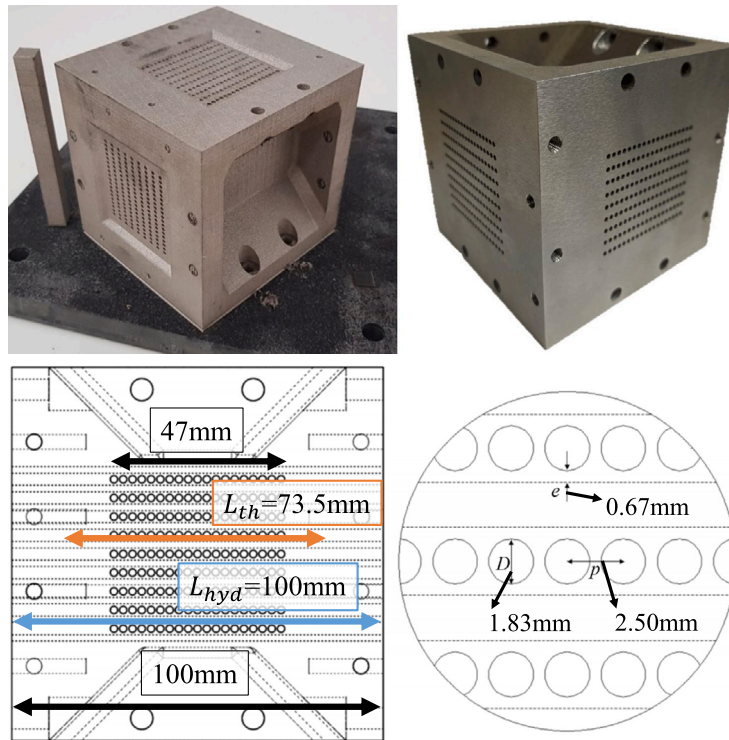


Fig. 8. Photos, geometries, and dimensions of the reference heat exchanger, from da Silva et al. [30].

$T_4 = T_1$, and $p_1 = p_4$. The thermal model is then run first, to refine the estimated outlet temperatures T_4 . Subsequently, the hydraulic model is executed, adopting the refined outlet temperatures to compute the pressure drops and update the inlet pressures p_1 . These updated pressures are then provided as new inputs for a second run of thermal model. The process is then repeated until the assumed values and computed results converge for both parameters. Finally, the volumetric–gravimetric performance is assessed, accounting for the refined mean fluid densities.

Ultimately, the following simulation outputs are returned by the model: the heat exchanged in a single plate-module, the total heat transfer of the HE, the total pressure drop of both fluids, the outlet temperatures, the upstream pressures, and the masses and volumes of all elements, both fluids and structure.

3.4. Model validation

A preliminary model validation is conducted against experimental data by Ref. [30], for a compact HE fabricated via AM. AISI 316

stainless steel is taken as the reference material for the component structure, with an average density of $\rho_s \approx 8000 \text{ kg m}^{-3}$ and a thermal conductivity of $k_s \approx 15 \text{ W m}^{-1} \text{ K}^{-1}$. An average surface roughness of $Ra = 12.21 \mu\text{m}$ is instead assumed for the channels, according to measurements by the authors.

For consistency, a representation of the test rig employed by da Silva et al. [30] is shown in Fig. 7; while geometries and dimensions of the reference heat exchanger are reported in Fig. 8.

A compact heat exchanger with a porosity σ of 0.1 is considered, consisting of 9 layers of hot fluid channels alternating with 10 layers of cold fluid channels. Each layer is made by a single row of 19 straight circular ducts with an average manufactured diameter of 1.83 mm. A 2.5 mm spacing separates the axes of the channels within a same layer, while an identical 2.5 mm gap is considered between the median planes of two adjacent layers. A hydraulic length L_{hyd} of 100 mm is assumed for pressure drop calculations (Eq. (20)), representing the total distance travelled by the fluids, equal, in this case, to the corresponding HE main dimensions: L_{HE} and W_{HE} .

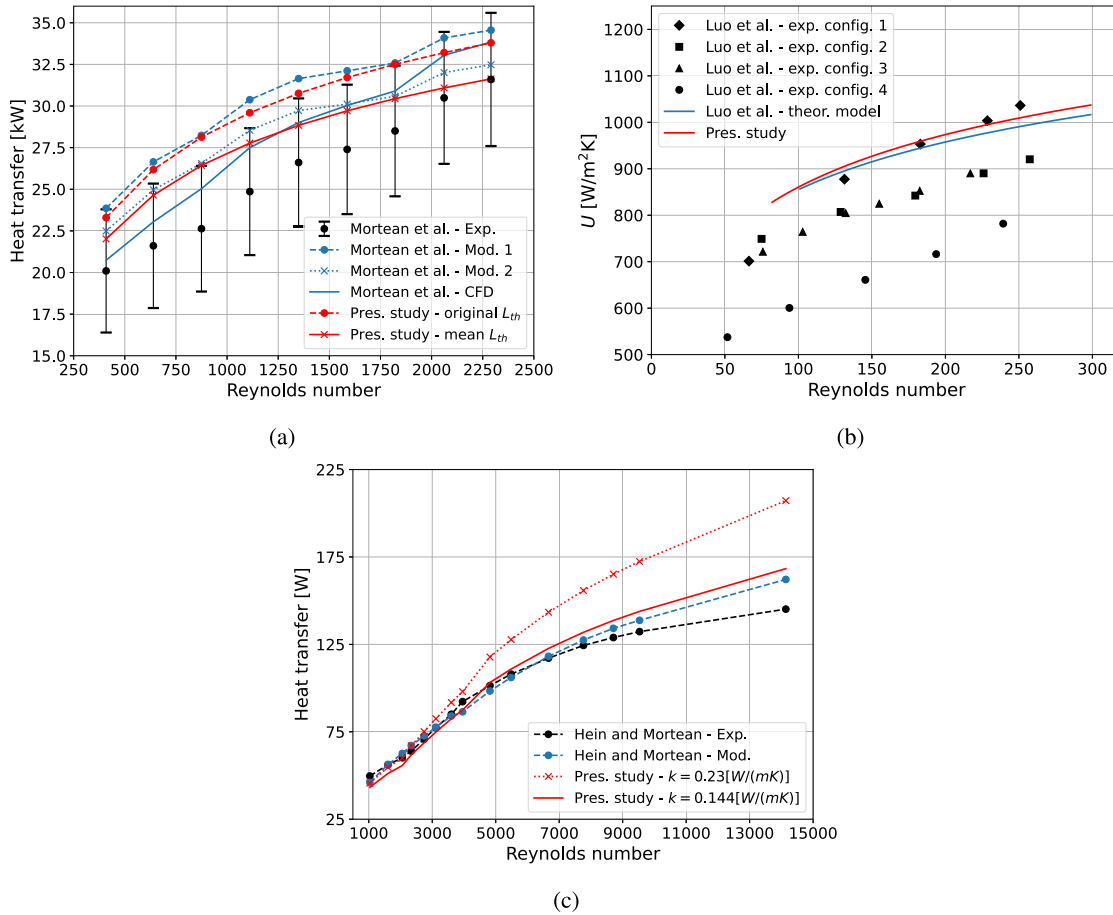


Fig. 9. Validation of the proposed thermal length definition against experimental data (black) and numerical predictions (blue) from Mortean et al. [56] 9(a), Luo et al. [57] 9(b), and Hein and Mortean [57] 9(c). Results from the present model are shown in red: the dashed line corresponds to simulations based on the reference heat transfer area adopted in the original studies, while the solid line uses the thermal length definition proposed by da Silva et al. [30]. In Fig. 9(c), da Silva et al.'s definition is consistently applied: the dotted line shows predictions using the reference study's thermal conductivity, while the solid line uses the EOS data sheet value for sintered Polyamide 2200.

Notably, experimental measurements for the reference geometry [30] were performed slightly upstream and downstream of the HE, due to practical constraints on sensor placement, as evidenced in Fig. 7. This introduced some additional pressure drops, which need to be accounted for in order to achieve a meaningful comparison between the simulation results and the empirical data. These additional losses are herein modelled accordingly to the formulations provided by the authors [30], as detailed in Appendix B. The resulting terms are then used to derive more accurate simulation inputs from the experimental measurements, omitting the influence of the test rig, and to calculate the pressure drops directly associated with the HE.

Additionally, following Ref. [30], a thermal length L_{th} of 73.5 mm is adopted to support thermal calculations. It is defined as the average between the full channel length of 100 mm, and the 47 mm section operating under true cross-flow conditions. This definition accounts for the heat transfer occurring in the regions surrounding the 47 mm true heat exchanger core, which would otherwise be neglected and underestimated. Conversely, assuming the entire HE (100 mm) as operating under ideal cross-flow conditions would be overly optimistic, and overestimate thermal performance, as demonstrated by da Silva et al. [30]. Given the component's symmetry, identical thermal lengths are assumed for both fluids, $L_{th,c}$ and $L_{th,h}$, and employed to define L_{plt} and W_{plt} in the numerical thermal model. On a practical level, Eqs. (7)–(10), along with the associated a and b parameters, remain unaffected by the thermal length definition. This occurs since the value of interest for these formulations is the $U L_{plt} W_{plt}$ product rather

than the plate dimensions themselves. This product is provided by the thermal resistance model, which instead strongly depends on the assumed value of L_{th} , particularly in Eqs. (16), (17), and (19), and when selecting the appropriate Nusselt formulation from Table 2.

For consistency, this thermal length definition is validated against data from Mortean et al. [56] for an AISI-316 compact heat exchanger manufactured via diffusion bonding. The reference geometry is a 167 mm × 167 mm water–water heat exchanger with 450 square channels of 3 mm side, arranged in 15 alternating layers. The proposed thermal model is employed to simulate the component's heat exchange using both the 0.9418 m² reference surface reported by the authors and the area derived from the thermal length definition of da Silva et al. [30]. Fig. 9(a) presents the results for both assumptions and compares them with the numerical predictions and experimental data of Mortean et al. [56].

The adopted thermal length definition is also validated against the experimental geometries by Luo et al. [57] and Hein and Mortean [58]. The work by Luo et al. [57] addresses the influence of flow (mal-) distribution in an aluminium cross-flow heat exchanger with 128 round channels across 8 layers, employing different inlet and outlet flow distributor configurations. The proposed model and thermal length definition are applied to this geometry, with the results shown in Fig. 9(b).

Hein and Mortean's study [58] investigates heat transfer in an AM compact heat exchanger featuring 84 round channels in 7 layers, fabricated via Selective Laser Sintering of Polyamide 2200. The

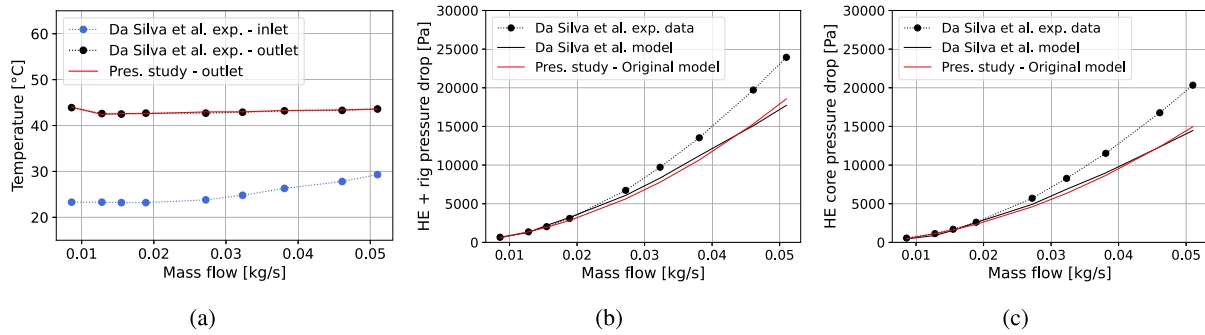


Fig. 10. Thermal-hydraulic results of the proposed integrated model (red line) compared to experimental data (black dotted line) and numerical predictions (black line) from Ref. [30]. 10(a) Inlet and outlet air temperature measurements and numerical results. 10(b) air pressure drop measurements and numerical results for the test rig. 10(c) air pressure drop measurements and numerical results for the sole heat exchanger (core).

results are compared for a thermal conductivity of $0.23 \text{ W m}^{-1} \text{ K}^{-1}$, as reported in the reference study, and $0.144 \text{ W m}^{-1} \text{ K}^{-1}$, consistent with the EOS technical data sheet for sintered Polyamide 2200 parts [59]. The simulation results for this geometry are presented in Fig. 9(c).

Results from Fig. 9(a) show that numerical predictions for the geometry by Morteau et al. [56] are consistent with other literature models, exhibiting comparable deviations and magnitudes. In particular, adopting the thermal length definition of da Silva et al. [30] yields the most accurate results and aligns with the more advanced models from the reference study [56], including finite element simulations. Regarding the component by Luo et al. [57], results from Fig. 9(b) demonstrate that the proposed model achieves satisfactory agreement with the theoretical predictions from the reference study. In particular, the results reasonably capture the experimental trends under highly uniform flow distribution (configuration 1). For the polymeric design by Hein and Morteau [58] (Fig. 9(c)), simulations assuming the reference thermal conductivity of $0.23 \text{ W m}^{-1} \text{ K}^{-1}$ do not closely match the experimental data. However, adopting a conductivity of $0.144 \text{ W m}^{-1} \text{ K}^{-1}$, as reported in the manufacturer's data sheet, yields predictions in acceptable agreement with the experiments.

These results support the validity of the proposed thermal model and thermal length definition, contributing to the validation of the presented methodology.

4. Results

Upon enhancing the model to account for the additional losses in the test rig and importing the reference HE geometries from Fig. 8, the component's thermal-hydraulic performance is simulated. Simulation outcomes are provided in Fig. 10 for the HE core and the test rig assembly, compared with the experimental data and numerical results from the authors [30].

Fig. 10(a) demonstrates a high consistency between this study's numerical results and the experimental data from Ref. [30] on the heat exchanger's thermal performance, with a maximum relative deviation of 1.4% on the temperature difference. These findings corroborate the validity of the assumptions adopted in extending the approach to the modelling of heat exchangers featuring circular ducts and an uneven number of channel layers, consolidating the intrinsic flexibility of the adopted thermal methodology. Additionally, these results evidence that the thermal length definition by da Silva et al. [30] is well suited for the modelling of heat exchanger plates through Eqs. (7)–(10).

Figs. 10(b) and 10(c) evidence, instead, a satisfactory agreement between this work's pressure drops predictions and those from Ref. [30]. Only minor differences are observed between the two, which are confirmed to derive from small variations in the actualization of the empirical loss coefficients. Consequently, however, the presented model also inherits the deviations of the original methodology from the experimental data, resulting in a pressure drop underestimation of up

to -22.4% for the test rig, and -26.4% for the HE core, particularly at higher Reynolds numbers.

Similar discrepancies exceed reasonable expectations for the employed methodology, which is based on well-established correlations for compact heat exchanger characterization [31]. Fabrication via additive manufacturing is instead the most likely cause of these inconsistencies, as accurate performance modelling of HEs for AM remains an active subject of investigation, as outlined by Careri et al. [20] and Karur and Singh [19]. In particular, issues with the accuracy and repeatability of the final product pose a major hindrance to the precise prediction of heat exchanger performance, due to variations in the component's dimensions, shapes, and roughness.

Da Silva et al. [30] addressed some of these issues, accounting for a high measured surface roughness of $12.21 \mu\text{m}$, and a significant shrinking in the manufactured channels diameters, which decreased from a design value of $D_{chan,design} = 2.00 \text{ mm}$ to a real fabricated value of $\bar{D}_{chan,AM} = 1.83 \text{ mm}$. These considerations resulted in the trends shown in Fig. 10 and maximum experimental deviation of 27%. Notably, a considerable relative roundness error of 0.08 was also observed for the channels. Ultimately, the study demonstrated a low influence of the surface roughness parameter on the calculated pressure drops. Ref. [60] confirms these results, highlighting a substantial impact of the channel diameter instead.

Notably, comparable diameter contractions and relative roundness errors were also observed by Kempen et al. [61], who provided explanations over the causes of these deformations. According to the authors, the creation of the melting pool is responsible for altering a components' dimensions, as it shifts the design profiles by an amount approximately equal to its radius. For internal structures, such as a channels, this shift results in the shape sizes being reduced by the magnitude of the melting pool diameter, suggesting that the reference heat exchanger was manufactured with a melting pool of about $170 \mu\text{m}$, provided shrinking from 2 mm to 1.83 mm. Additionally, Ref. [61] also observed the formation of dross on the channels' ceilings, whenever these were not built with their axes perpendicular to the platform. This dross originated from an uneven cooling of the melting pool into lower layers of unsintered powder, resulting in a protrusion roughly the size of the melting pool diameter, and the significant relative roundness error.

For a melting pool diameter of $170 \mu\text{m}$ and an average channel diameter of 1.83 mm, as the ones of the reference heat exchanger, the formation of a similar dross results in a relative roundness error of 0.09, which complies with the 0.08 value declared by da Silva et al. [30].

4.1. Corrected pressure drop formulation

The definition of a corrective factor gravitating around the formation of the AM dross is herein proposed, as the relative roundness error of the channels, while opportunely mentioned in Ref. [30], does not seem to be reflected in the hydraulic model at the current stage. The

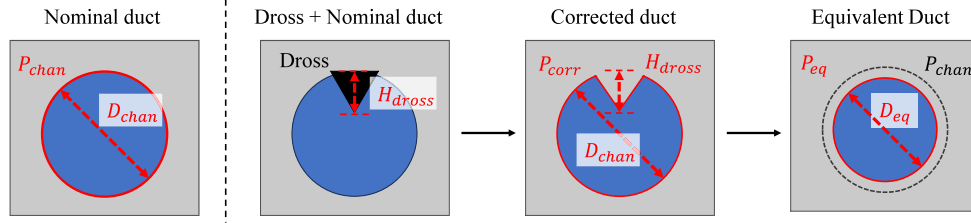


Fig. 11. Functional scheme of the corrected channels' sections, accounting for the presence of a triangular shaped laser melting dross at the top of the duct.

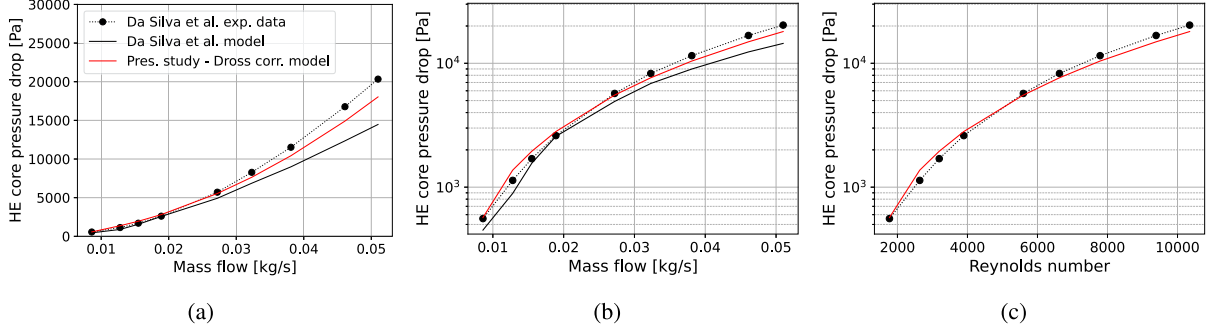


Fig. 12. Hydraulic results of the dross-corrected model (red line) compared to experimental data (black dotted line) and simulation outcomes (black line) by da Silva et al. [30]. Detail of the air pressure drops of the heat exchanger core with respect to the fluid mass flow rate in linear 12(a) and logarithmic 12(b) scales, and for the Reynolds numbers in logarithmic scale 12(c).

presence of a triangular-shaped dross is therefore assumed at the top of the channels, taking an isosceles right triangle and an equilateral triangle as two possible approximations of the dross geometry. Then, the area filled by the dross is subtracted from the region otherwise occupied by a perfectly round duct, to define a corrected cross-sectional area, according to Eq. (29), as shown in Fig. 11.

$$\begin{cases} A_{corr} = \frac{\pi}{4} D_{chan}^2 - H_{dross}^2 & \text{for isosceles right triangle} \\ A_{corr} = \frac{\pi}{4} D_{chan}^2 - \frac{\sqrt{3}}{3} H_{dross}^2 & \text{for equilateral triangle} \end{cases} \quad (29)$$

Where H_{dross} is the height of the dross, that is assumed equal to melting pool diameter (170 μm). Similarly, a corrected cross-sectional perimeter is defined according to Eq. (30).

$$\begin{cases} P_{corr} \approx \pi D_{chan} + 2H_{dross}(\sqrt{2} - 1) & \text{for isosceles right triangle} \\ P_{corr} \approx \pi D_{chan} + \frac{2}{3}\sqrt{3}H_{dross} & \text{for equilateral triangle} \end{cases} \quad (30)$$

A corrected hydraulic diameter is determined for the adjusted channels' area and perimeter, $D_{hyd,corr} = 4 \cdot A_{corr} / P_{corr}$. This hydraulic diameter is then assumed to define an equivalent circular geometry to be employed for the hydraulic calculations, according to Eq. (31).

$$\begin{cases} D_{eq} = D_{hyd,corr} \\ P_{eq} = \pi D_{eq} \\ A_{eq} = \pi/4 D_{eq}^2 \end{cases} \quad (31)$$

Provided the reference geometry of $D_{chan} = 1.83 \text{ mm}$, both dross shapes result in a comparable hydraulic diameter reduction of about $3.7\% \pm 0.2\%$ are thus treated as equivalent in the following analysis. Pressure drops are recalculated assuming this new corrected diameter, with the corresponding results being presented in Fig. 12. A stronger correlation can be observed overall and especially at higher Reynolds numbers, where the maximum pressure drop underestimation is reduced from 26.4% to 11.4% with respect to the original formulation.

Additionally, an alternative formulation is proposed, introducing an uncertainty factor K_p to the HE core pressure drop calculation, as shown in Eq. (32).

$$\Delta p_{core,corr} = K_p \Delta p_{core} \quad (32)$$

This equation provides a more conservative estimate of the HE's hydraulic losses, preserving a strong correlation with the component's geometries, while retaining the channel's nominal hydraulic diameter. Fitting the equation to experimental data from Ref. [30] resulted in a preliminary corrective factor of $K_p = 1.3$. Results of pressure drop calculation according to this new formulation are provided in Fig. 13 demonstrating stronger correlation at higher Reynolds numbers, with the maximum pressure drop underestimation being reduced to only 4.3%.

Notably, both corrective formulations lead to a significant increase in the simulated pressure drops at lower Reynolds numbers, resulting in overestimations of the hydraulic losses, especially near the transitional flow region. This effect is most evident with the second formulation (Eq. (32)), which exhibits a maximum relative deviation of 30.8% around Reynolds numbers of 2500. Nonetheless, the corrected formulations remain well-suited for this study, as the corresponding absolute errors in these regions are small, resulting in negligible practical impact. In contrast, the significant reduction in pressure drop underestimation at higher Reynolds numbers improves accuracy of the results in absolute terms, addressing operational regions that are, instead, critical to HE performance.

A comparison between the pressure drops resulting the original, dross-corrected, and penalty factor-corrected models is provided in Fig. 14.

The effects of both corrections on the model's thermal results are detailed in Fig. 15. However, since the reference outlet temperatures from Fig. 10(a) are all very similar, Eq. (33) is applied to the experimental measurements from Ref. [30] to extract the real component heat transfer rate, and highlight numerical deviations in the models.

$$q = \dot{m} \cdot c_p (T_{out} - T_{in}) \quad (33)$$

Results from Fig. 15 evidence a slight increase in the thermal model's deviations for the dross-corrected formulation. By contrast, use of the K-factor shows negligible impact on the simulated outlet temperatures, closely matching outcomes from the original model. This behaviour emerges as the reduced channel sections from the dross corrected shapes drives minor increases in the computed Reynolds numbers, leading to slight heat transfer overestimation. Nonetheless, the maximum relative deviation in the cold fluid's temperature change

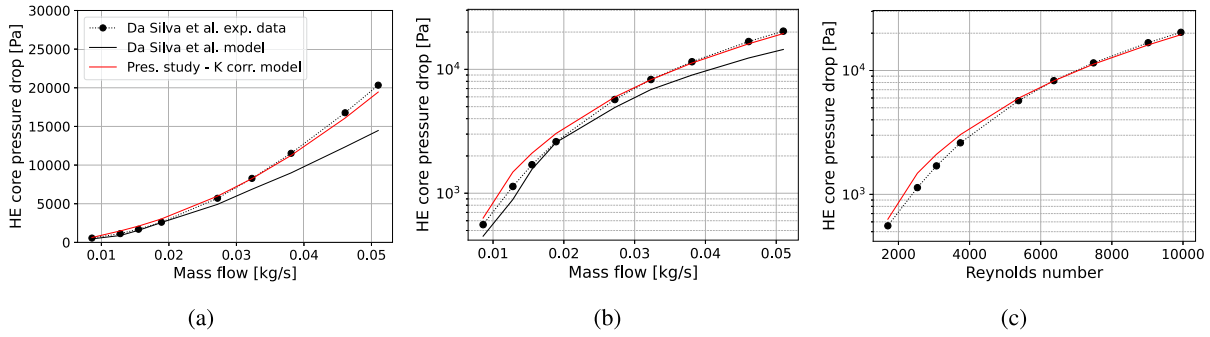


Fig. 13. Hydraulic results of the K_p -corrected model (red line) compared to experimental data (black dotted line) and simulation outcomes (black line) from Ref. [30]. Detail of the air pressure drops of the heat exchanger core with respect to the fluid mass flow rate in linear 13(a) and logarithmic 13(b) scales, and for the Reynolds numbers in logarithmic scale 13(c).

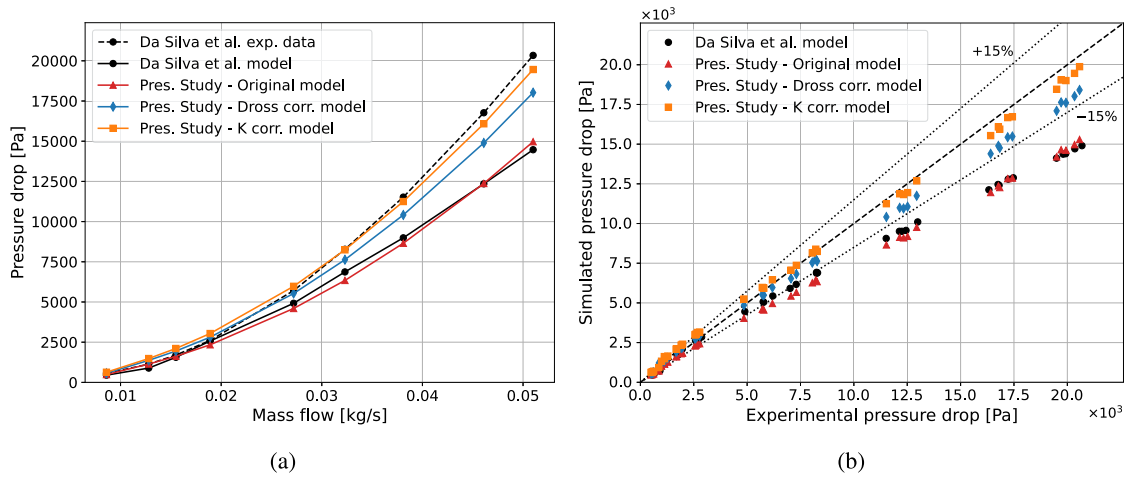


Fig. 14. Comparison of results from the various models simulating the air pressure drops in the core HE from Ref. [30]. Detail of trends with respect to the air mass flow rates 14(a) and experiential deviations 14(b).

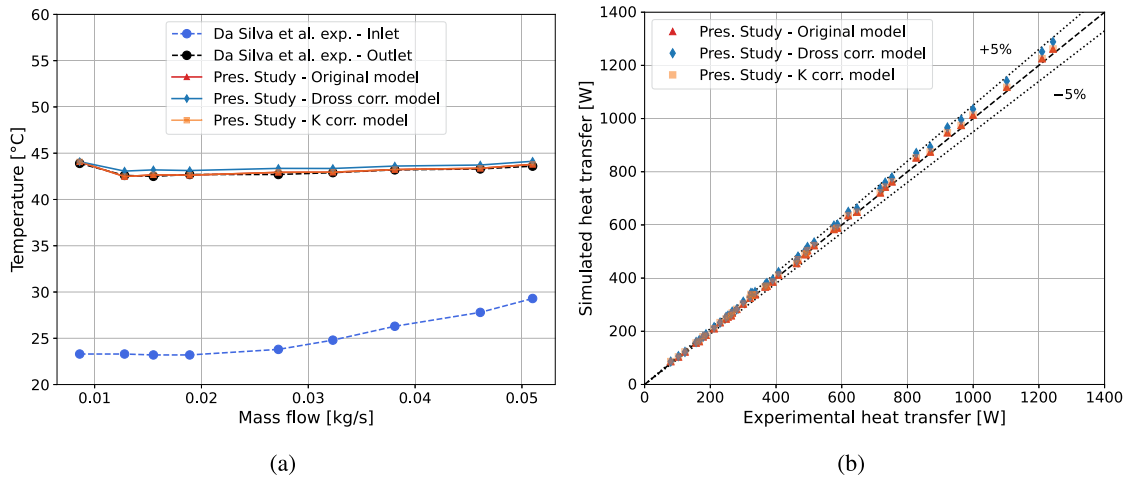


Fig. 15. Model's thermal results following the application of corrective formulations: detail of the outlet temperature trends 15(a) and experiential deviations of the associated heat transfer rates 15(b).

only increases from 1.4% to 3.7% following the application of the proposed shape correction, hence remaining well below the commonly accepted 5% accuracy threshold.

4.2. Computational cost analysis

Ultimately, the computational costs of the proposed ϕ -based thermal model are compared against alternative discretized approaches

from the literature. The finite difference routine for unmixed heat transfer in cross-flow plates by Nellis and Klein [62] is adapted for implementation in Python and serves as a benchmark. The algorithm defines a virtual mesh of $M \times N$ grid points ($M = N$), initialized with uniform temperature distributions for both fluids. Fluid properties are evaluated locally at each grid point using the CoolProp library [55]. Then, the local energy balance is computed between consecutive mesh points according to Eq. (34), and the resulting temperature fields are

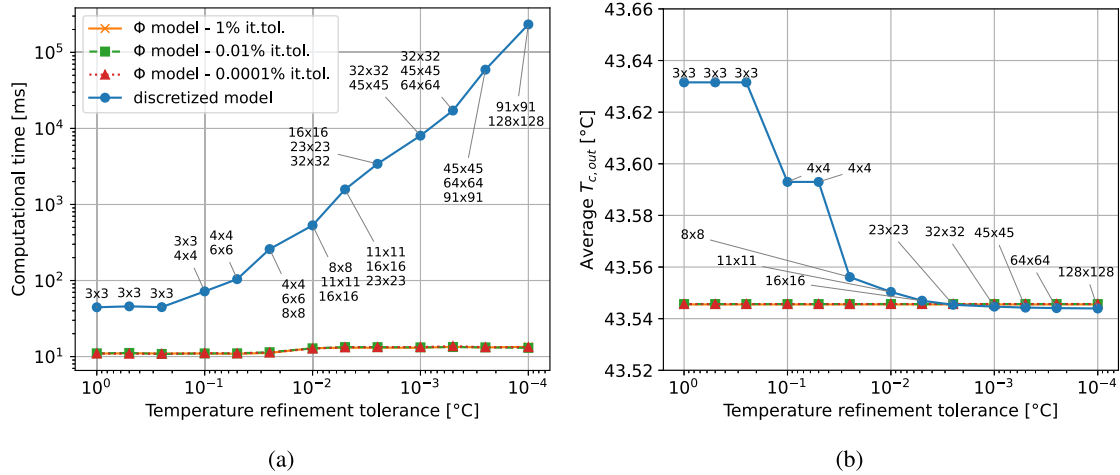


Fig. 16. Comparison of the average computational costs 16(a) and reference simulation outcomes 16(b) for the proposed global ϕ -model and a finite difference approach, as a function of the temperature refinement tolerance. Global model results are provided for three minimum summation refinement thresholds in solving the ϕ equation: 1%, 0.01%, 0.0001%. The converged mesh sizes associated with each tolerance are also reported.

updated accordingly. This process repeats until the root-mean-square error between two successive temperature fields falls below a predefined tolerance. Similarly to the ϕ -model, this convergence threshold is set to 0.01 °C by default.

$$\begin{cases} \frac{\dot{m}_h c_{p,h}}{M} (T_{h_{i,j}} - T_{h_{i,j+1}}) = \frac{UA}{MN} \left[\frac{T_{h_{i,j}} + T_{h_{i,j+1}}}{2} - \frac{T_{c_{i,j}} + T_{c_{i+1,j}}}{2} \right] \\ \frac{\dot{m}_c c_{p,c}}{N} (T_{c_{i+1,j}} - T_{c_{i,j}}) = \frac{UA}{MN} \left[\frac{T_{h_{i,j}} + T_{h_{i,j+1}}}{2} - \frac{T_{c_{i,j}} + T_{c_{i+1,j}}}{2} \right] \end{cases} \quad (34)$$

For $i = 1, \dots, M$ and $j = 1, \dots, N$.

Additionally, an automatic mesh refinement routine is introduced to tailor the discretization to the desired solution accuracy while limiting computational costs. Starting from an initial 2×2 mesh, the number of grid points is progressively increased following Eq. (35), effectively doubling the resolution at each step. After each refinement, the average outlet temperatures are recomputed and compared with those from the previous mesh. The process is repeated until the outlet temperature difference between two successive meshes falls below a user-defined refinement tolerance, which is also set by default to 0.01 °C.

$$M_n = \text{round}(M_0 r^n) \quad \text{With: } M_0 = 2, \quad r = \sqrt{2}, \quad n = 0, 1, 2, 3, \dots \quad (35)$$

It is important to note that two different tolerances guide the solution of the discretized model: one controls the iterative convergence of the temperature fields within a given mesh, while the other evaluates convergence between successive mesh refinements, determining whether higher resolution is required. However, for simplicity, a single temperature refinement tolerance is defined and applied to both criteria. Consequently, choosing a looser tolerance (e.g., 0.1 °C) will result in a coarser mesh grid and in a less strict convergence of the temperature fields. Contrarily, aiming for a tighter tolerance (e.g. 0.001 °C) will demand finer meshes and more accurate fluid mapping.

A simulation campaign compares the computational costs of this discretized thermal approach with those of the proposed ϕ -model, considering temperature refinement tolerances between 1 °C and 0.0001 °C for both methods. Each model is run 100 times per each tolerance target, assuming 0.2656 kg s⁻¹ of hot water at 60 °C and 0.0278 kg s⁻¹ of cold air at 25 °C, with the inlet reference temperatures being randomized by ± 10 °C for a more robust estimate. Additionally, results of the proposed global model are compared for three different iteration refinement thresholds when solving the ϕ equation (Eq. (7)): 1%, 0.01%, 0.0001%.

The results of this study are presented in Fig. 16, highlighting the models' average computational cost over 100 simulations and the computed cold-fluid outlet temperature for the reference, non-randomized case.

Results from Fig. 16(a) confirm the substantially lower computational cost of the proposed global ϕ -model compared to the discretized approach. Specifically, for temperature refinement tolerances exceeding 0.1 °C, the ϕ -model requires, on average, only 25% of the time employed by the finite-difference method. More importantly, while the computational cost of solving the ϕ equation increases only marginally as the tolerance is tightened, the runtime of the discretized approach grows exponentially consequent to the need for finer meshes and additional iterations. Particularly, for the adopted reference tolerance of 0.01 °C, the global ϕ -model requires only about 2% of the total computational time of the discretized model.

Notably, the ϕ -model's runtime remains nearly unchanged across the three tested summation accuracies (1%, 0.01%, 0.0001%), confirming the negligible impact of solving the ϕ equation itself. In practice, Eq. (7) converged with only 2, 3, and 4 summation terms for iteration thresholds of 1%, 0.01%, and 0.0001%, respectively.

Fig. 16(b) presents the numerical outcomes of both models for the reference simulation conditions, excluding the inlet temperature randomization. The discretized model shows significant numerical convergence once the mesh grid exceeds a 10×10 resolution, consistent with analyses from Nellis and Klein [62]. For the presented routine, this is achieved when the temperature refinement tolerance is smaller than 0.01 °C.

By contrast, the ϕ -model is considerably less sensitive to said tolerance, providing accurate and nearly identical predictions across the entire range. This occurs because, in the ϕ -model, the temperature refinement tolerance only affects the determination of global fluid properties, unlike in the discretized model, where it also dictates the mesh resolution and the overall accuracy of the solution. The accuracy of the global ϕ -model is instead controlled by the minimum summation term threshold regulating the iterations on the ϕ value. Notably, all three tested thresholds (1%, 0.01%, and 0.0001%) result in comparable numerical outcomes, indicating that the first two terms of the ϕ summation already capture most of the heat transfer phenomenon.

5. Conclusions

This study presents a renewed, integrated modelling approach for the simulation of high-performance heat exchangers for Additive Manufacturing, featuring rectangular and circular channels in a cross-flow

configuration. It aims to provide a robust, flexible, and efficient numerical tool to support future design optimization workflows for heat exchangers in transport systems. Particularly, this work investigates the component's thermal, hydraulic, and gravimetric behaviours and validates them against experimental data from the literature, achieving good results correspondence. Finally, it addresses the challenges of accurately modelling hydraulic losses in additively manufactured components, and proposes two preliminary corrective formulations that reduce the deviation in pressure drop predictions, bringing the experimental deviation at higher Reynolds numbers below 15%.

The key findings of this study are summarized in the following:

- A revised 1-D modelling approach is developed for the rapid assessment of heat exchangers' performance in the context of additive manufacturing. The following behaviours are considered: thermal, hydraulic, volumetric, and gravimetric. The methodology focuses primarily on physics-driven formulations, minimizing reliance on empirical correlations or discretization to enable flexible yet computationally efficient simulations. Extensive parametrization ensures the model's adaptability to changes in the geometries, while a careful selection of modelling strategies and a modular tool design support future extension and enhancements, particularly for alternative shapes and configurations.
- The theoretical framework proposed by Nacke et al. [34] serves as the basis for the thermal characterization of the HE, condensing discretized contributions into a single formulation to avoid solving full CFD problems and reduce computational costs. This framework is successfully extended to describe the geometry presented by da Silva et al. [30]. The thermal length L_{th} definition introduced by da Silva et al. is effectively employed to parametrize the plate model by Nacke et al. confirming consistency of the assumption with respect to alternative modelling strategies. Finally, a hypothesis is introduced to treat any additional channel layers within the HE as adiabatic when an uneven number of layers exists between the hot and cold fluids. This assumption yields strong agreement between simulations and experiments, extending the pre-existing methodology.
- A robust numerical implementation is developed. The hydraulic model is designed to calculate the pressure drops starting from the outlet and then moving upstream, to prevent numerical issues and support future use in optimization loops. The Churchill formulation is adopted for the determination of the Darcy friction factor f_D , as it provides an explicit expression valid across all flow regimes without discontinuities. An iterative loop is implemented to solve the infinite sum term in the ϕ equation of the thermal model, which calculates downstream properties starting from the inlet section. A dedicated integration script combines these two models into a unified methodology, employing an iterative loop to refine unknown simulation variables. This approach enables complete characterization of the heat exchanger using only three thermo-hydraulic inputs: inlet temperatures, outlet pressures, and mass flow rates. The tool is also made highly modular allowing for future upgrades and optimization purpose.
- Numerical validation of the proposed methodology is performed using the additively manufactured heat exchanger from Ref. [30]. The thermal model exhibits remarkable consistency with the experimental data, achieving a maximum error of 1.4% on the computed temperature change. In contrast, a significant relative deviation of 26.4% is observed for the hydraulic model, resulting in major underestimation of the pressure drops at higher Reynolds numbers. A probable cause for these inconsistencies was identified in the high relative roundness errors of the reference component channels, likely due to the formation of manufacturing dross on the channels' ceilings. Two corrective formulations are proposed to account for this phenomenon: one defines a corrected hydraulic diameter proportional to the dross and the

other applies a conservative uncertainty factor regressed on data from Ref. [30]. The first approach reduces the maximum pressure drop underestimation to 11.4% while the second achieves a reduction to 4.3%. The thermal results are marginally affected by these changes, with the dross corrected formulation increasing the maximum heat transfer deviation to 3.7%, and the K -corrected equation retaining a 1.4% deviation.

Limitations of the presented approach include some inconsistencies with pressure drop prediction close to transitional flow regimes, where both corrected formulations observe major losses overestimation.

Nonetheless, the magnitude of these deviations remains small in absolute terms and does not compromise the validity of the results presented in this work. Future studies should aim to address these issues, and pursue a more exhaustive validation of the proposed corrective correlations to better define their applicability ranges and ultimately, refine the regression.

Possible future applications of the proposed numerical approach comprise rapid performance assessment of radiators, support for HE design exploration, and application inside virtual optimization workflows for enhanced component design. Additionally, there is strong potential for integrating the proposed methodology with Additive Manufacturing workflows, extending fast numerical design conceptualization into rapid prototyping.

CRediT authorship contribution statement

Stefano Favre: Writing – review & editing, Writing – original draft, Visualization, Validation, Software, Methodology, Formal analysis, Conceptualization. **Daide Di Blasio:** Writing – review & editing, Writing – original draft, Visualization, Validation, Supervision, Resources, Methodology, Formal analysis, Conceptualization. **Tom Fletcher:** Writing – review & editing, Supervision, Resources, Methodology, Conceptualization. **Eugenio Brusa:** Writing – review & editing, Supervision, Resources, Funding acquisition, Conceptualization. **Cristiana Delprete:** Writing – review & editing, Supervision, Resources.

Funding

This publication is part of the project PNRR-NGEU which has received funding from the Italian Ministry of University and Research (MUR) - DM352/2022 (CUP n° E12B22000560006).

Declaration of competing interest

The authors declare that they have no known competing financial interests or personal relationships that could have appeared to influence the work reported in this paper.

Appendix A. Nusselt formulations

The convective heat transfer coefficients of the fluids h_{conv} are evaluated via the mutually exclusive, empirical formulations provided in Table 2.

The selection of an adequate equation is based on several factors, with the boundary layer playing a major role. A fundamental distinction exists between expressions suited for the modelling of a flat plate, where the boundary layer is presumed unaffected by external constraints; and those intended for closed-channel geometries, which instead assume merging of two boundary layers generated on opposing walls. Subsequently, the flow regime can be classified as either turbulent, laminar, or transitional.

The works of Mudawar et al. [34,35] consider boundary layer merging whenever the maximum boundary layer thickness exceeds half

Table 2
Nusselt formulations and convective heat exchange coefficients of fluids.

Equation	Notes
Finned-plate hypothesis: $\overline{Nu} = \frac{\bar{h}L_{th}}{k_f}$	Valid for: $\delta_{bl} < H_{chan}/2$ & $\delta_{bl} < B_{chan}/2$ (H_{chan} and B_{chan} substituted by D_{chan} for circular channels), Assuming: $Re = \frac{\rho u L_{chan}}{\mu}$ & $Pr = \frac{c_p \mu}{k_f}$
$\overline{Nu} = 0.664 Re^{1/2} Pr^{1/3}$ [23]	When $Re < Re_{crit}$
$\overline{Nu} = \left[0.664 Re_{crit}^{1/2} + 0.037 \left(Re^{4/5} - Re_{crit}^{4/5} \right) \right] Pr^{1/3}$ [23]	When $Re \geq Re_{crit}$
Closed-channel hypothesis: $\overline{Nu} = \frac{\bar{h}D_{hyd}}{k_f}$	Valid for: $\delta_{bl} \geq H_{chan}/2$ & $\delta_{bl} \geq B_{chan}/2$ (H_{chan} and B_{chan} substituted by D_{chan} for circular channels), Assuming: $Re = \frac{\rho u D_{hyd}}{\mu}$ & $Pr = \frac{c_p \mu}{k_f}$ & $D_{hydr} = \frac{4A_{lam}}{P_{con}}$
$\overline{Nu} = 4.364$ [63]	When $Re < 2300$ & - Laminar flow - Fully developed
$\overline{Nu} = 1.953 \left(\frac{1}{l_n} \right)^{1/3}$ [64]	When $Re < 2300$ & - Laminar flow - Thermally in development & $l_{th} \leq 0.03$ m
$\overline{Nu} = 4.364 + 0.0722 \left(\frac{1}{l_n} \right)$ [64]	When $Re < 2300$ & - Laminar flow - Thermally in development & $l_{th} \geq 0.03$ m
$\overline{Nu} = \left[4.364^3 + 0.6^3 + a_{Nu}^3 + b_{Nu}^3 \right]^{1/3}$	When $Re < 2300$ & - Laminar flow - Hydro-dynamically and thermally in development
$a_{Nu} = 1.953 \sqrt[3]{Pr Re (D_{hyd}/L_{hyd})} - 0.6$	
$b_{Nu} = 0.924 \sqrt[3]{Pr^2 Re (D_{hyd}/L_{hyd})}$ [65]	
$\overline{Nu} = (Nu_{lam}^6 + Nu_{urb}^6)^{1/6}$	When $1800 \leq Re < 4000$ - Transitional flow
$Nu_{lam} = 4.364 + \frac{0.086(1/L_n)^{1.33}}{1+0.1Pr(ReD_n/L_{hyd})^{0.83}}$	
$Nu_{urb} = \frac{(f/8)(Re-1000)Pr}{1+12.7(f/8)^{1/2}(Pr^{2/3}-1)}$ $f = \frac{1}{4} (1.8 \log Re - 1.5)^{-2}$	
[66]	
$\overline{Nu} = \frac{(f/8)(Re-1000)Pr}{1+12.7(f/8)^{1/2}(Pr^{2/3}-1)} \left(1 + \left(\frac{L_{hyd}}{D_{hyd}} \right)^{-2/3} \right)$	When $Re \geq 4000$ - Turbulent flow
$f = \frac{1}{4} (1.8 \log Re - 1.5)^{-2}$ [23,67,68]	

the distance to the opposing wall. By contrast, Nusselt correlations for heat transfer over a flat surface are effectively employed to model an interrupted fin pattern specifically intended to favour boundary layer disruption. The Blasius equations, adapted through the work of Schlichting [69], are here employed to determine the boundary layer thickness perpendicular to the surface, according to Eq. (36).

$$\begin{cases} \delta_{bl} \simeq 5x Re_x^{-1/2} & \text{if } Re_x < 2300 \text{ (laminar)} \\ \delta_{bl} \simeq 0.37x Re_x^{-1/5} & \text{if } Re_x > 2300 \text{ (turbulent)} \end{cases} \quad (36)$$

Where Re_x expresses the Reynolds number of the fluid at a given point x , which is set equal to the reference length of the channels to determine the maximum registered layer thickness.

Influence the entrance region is considered for all internal flow regimes. However, laminar flow equations are further subdivided into fully developed flow, thermally in development flow, and hydro-dynamically & thermally in development flow to simplify computation when adequate flow conditions are met. A fluid flow is considered hydrodynamically fully developed whenever the channel's dimensionless hydrodynamic length l_{hyd} , defined according to Eq. (37), exceeds the hydrodynamic input length Z_{hyd} . This threshold equals 0.056 for laminar flow in circular ducts, 0.09 for laminar flow in square channels [70], and 1.359 for turbulent flow in circular passages [71].

$$l_{hyd} = \frac{L_{hyd}/D_{hyd}}{Re} \quad (37)$$

Where L_{hyd} corresponds to actual channels' hydraulic length, here equivalent to the total channel length and the associated HE dimension: $L_{hyd,h} = L_{chan,h} = W_{HE}$, and $L_{hyd,c} = L_{chan,c} = L_{HE}$. Similarly, a flow is considered thermally fully developed whenever the channel's dimensionless thermal length l_{th} , defined according to Eq. (38), exceeds the input length Z_{th} . This value is equal to 0.05 [31] in circular ducts and 0.06204 in square channels [72].

$$l_{th} = \frac{L_{th}/D_{hyd}}{RePr} \quad (38)$$

Where, the channels' thermal length L_{th} represents a virtual dimension functional to the modelling of a HE's heat transfer, roughly indicating the portion of the ducts involved with the heat exchange. Da Silva et al. [30] demonstrated that the most accurate results are obtained by approximating a fluid's thermal length as the average between its hydraulic length L_{hyd} and the length of the portion effectively involved with pure cross-flow heat transfer.

Appendix B. Additional pressure drop terms of the test rig

The experimental test rig by da Silva et al. [30], employs a series of components to connect the heat exchanger with the instrumentation performing the readings. These elements are attached to the tested component, forming an assembly that includes: two manifolds, housing the sensors and linking the assembly to the rest of the rig; and two headers, joining the manifolds with the heat exchanger. However, each of these elements also introduces a pressure drop which is inevitably registered in the experimental measurements, and needs to be accounted for in the simulation. Modelling of these additional losses is performed with respect to some relevant sections in the assembly, as shown in Fig. 17. These are: sections 0 and 5, representing the sensor locations and the assembly boundaries; and sections 1' and 4', designating the connection between the headers and the manifolds.

Pressure drops in the headers are computed through Eq. (39) for the inlet, and Eq. (40) for the outlet, according to Idel'Chik [73]. The irreversibility coefficients are set to $\zeta_{exp} = 0.5$ for the inlet, and $\zeta_{con} = 0.25$ to 0.097, for the outlet, in line with Ref. [30], with $\zeta_{exp} = 0.25$ applying to the lowest Reynolds numbers and $\zeta_{exp} = 0.097$ to the highest.

$$\Delta p_{1'1} = \Delta p_{header_{in}} = \frac{\rho_1 u_1^2}{2} \left[1 - \left(\frac{A_1}{A_{1'}} \right)^2 + \zeta_{exp} \right] \quad (39)$$

$$\Delta p_{4'4} = \Delta p_{header_{out}} = \frac{\rho_4 u_4^2}{2} \left[\left(\frac{A_4}{A_{4'}} \right)^2 - 1 + \zeta_{con} \right] \quad (40)$$

Pressure drops in the manifolds are instead determined through Eqs. (41) and (42) for the inlet and outlet respectively, following Çengel and Cimbala [74]. A loss coefficient of $K_L = 0.53$ is assumed for both equations, in line with the one proposed by the authors [30].

$$\Delta p_{01'} = \Delta p_{MLin} = \frac{\rho_0 K_L u_0^2}{2} \quad (41)$$

$$\Delta p_{4'5} = \Delta p_{MLout} = \frac{\rho_5 K_L u_5^2}{2} \quad (42)$$

The total pressure drop measured by the test rig is thus obtained by combining the additional loss terms with the ones of heat exchanger core, according to Eq. (43).

$$\Delta p_{rig} = \Delta p_{MLin} + \Delta p_{header_{in}} + \Delta p_{core} + \Delta \Delta p_{header_{out}} + \Delta p_{MLout} \quad (43)$$

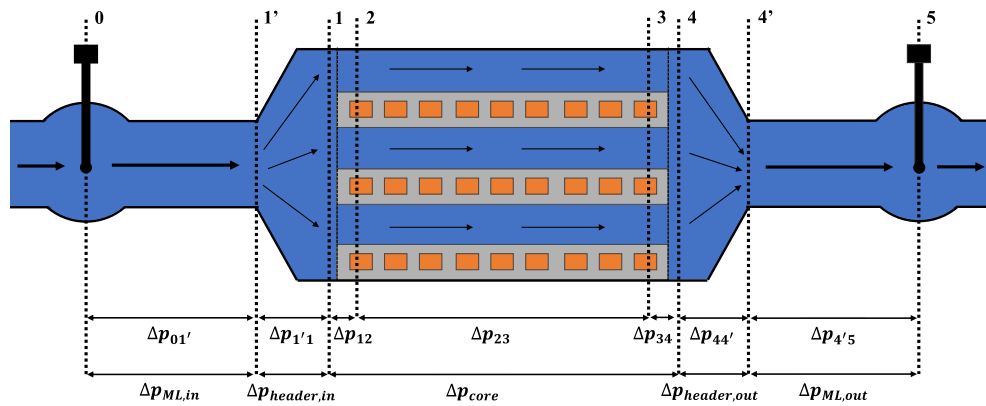


Fig. 17. Heat exchanger core, headers, and manifolds representation, with the associated sections of interest for pressure drop evaluation, according to the test rig presented Ref. [30].

Ultimately, the additional pressure drop terms can also be employed individually to refine the input parameters of the simulation, $p_0 \rightarrow p_1$ and $p_5 \rightarrow p_4$, while opportune rearrangement of Eq. (43) allows for the experimental Δp_{core} to be extracted for comparison.

Data availability

Data will be made available on request.

References

- [1] United Nations, Transforming our world: The 2030 agenda for sustainable development. Resolution adopted by the general assembly on 25 september 2015 (A/RES/70/1), 2015, <https://docs.un.org/en/A/RES/70/1>. (Accessed 15 July 2025).
- [2] European Commission, Directorate-General for Mobility and Transport, Sustainable and smart mobility strategy – putting European transport on track for the future, 2020, <https://eur-lex.europa.eu/legal-content/EN/TXT/?uri=CELEX:52020DC0789>. (Accessed 15 July 2025).
- [3] M. Muratori, T. Kunz, A. Hula, M. Freedberg, U.S. National Blueprint for Transportation Decarbonization: A Joint Strategy to Transform Transportation, Tech. Rep. DOE/EE-2674, United States. Department of Energy. Office of Energy Efficiency and Renewable Energy, 2023, <http://dx.doi.org/10.21949/7ddb-kt28>.
- [4] European Commission, Towards zero emission road transport (2zero) partnership, 2021, <https://www.2zeroemission.eu/>. (Accessed 15 July 2025).
- [5] J. Tian, P. Wang, D. Zhu, Overview of Chinese new energy vehicle industry and policy development, Green Energy Resour. 2 (2) (2024) 100075, <http://dx.doi.org/10.1016/j.gerr.2024.100075>.
- [6] Zero Emissions Ship Technology Association (ZESTAs), ZESTAs official website, 2025, <https://zestas.org/>. (Accessed 15 July 2025).
- [7] European Commission, Co-programmed partnership on zero-emission waterborne transport: Proposal and strategic research & innovation agenda, 2021, https://research-and-innovation.ec.europa.eu/system/files/2020-05/european_partnership_for_zero-emission_waterborne_transport.pdf. (Accessed 15 July 2025).
- [8] U.S. Environmental Protection Agency, Clean ports program: Overview of zero-emission technology deployment, 2024, <https://www.epa.gov/ports-initiative/cleanports>. (Accessed 15 July 2025).
- [9] S. Chen, C. Miao, Q. Zhang, Understanding the evolution of China's green shipping policies: Evidence by social network analysis, J. Clean. Prod. 482 (2024) 144204, <http://dx.doi.org/10.1016/j.jclepro.2024.144204>.
- [10] Clean Aviation Joint Undertaking, Clean Aviation, Highlights 2023 – Towards Disruptive Technologies for Aircraft by 2035, Publications Office of the European Union, 2024, <http://dx.doi.org/10.2886/0905205>.
- [11] National Aeronautics and Space Administration (NASA), NASA Strategic Plan FY 2022: Strategic Objective 3.2 – Advance Aeronautics Research to Transform Aviation and Enable a Sustainable Future, Tech. Rep., NASA, Washington, D.C., 2022, (Accessed 15 July 2025).
- [12] Q. Wang, B. Jiang, B. Li, Y. Yan, A critical review of thermal management models and solutions of lithium-ion batteries for the development of pure electric vehicles, Renew. Sustain. Energy Rev. 64 (2016) 106–128, <http://dx.doi.org/10.1016/j.rser.2016.05.033>.
- [13] Y. Wang, Q. Gao, G. Wang, P. Lu, M. Zhao, W. Bao, A review on research status and key technologies of battery thermal management and its enhanced safety, Int. J. Energ. Res. 42 (13) (2018) 4008–4033, <http://dx.doi.org/10.1002/er.4158>.
- [14] S.G. Kandlikar, Z. Lu, Thermal management issues in a PEMFC stack – A brief review of current status, Appl. Therm. Eng. 29 (7) (2009) 1276–1280, <http://dx.doi.org/10.1016/j.applthermaleng.2008.05.009>, Selected Papers from the 10th UK National Heat Transfer Conference, Edinburgh, Scotland, September 10–11, 2007.
- [15] Y. Wang, D.F. Ruiz Diaz, K.S. Chen, Z. Wang, X.C. Adroher, Materials, technological status, and fundamentals of PEM fuel cells – A review, Mater. Today 32 (2020) 178–203, <http://dx.doi.org/10.1016/j.mattod.2019.06.005>.
- [16] S. Ma, M. Jiang, P. Tao, C. Song, J. Wu, J. Wang, T. Deng, W. Shang, Temperature effect and thermal impact in lithium-ion batteries: A review, Prog. Nat. Sci. Mater. Int. 28 (6) (2018) 653–666, <http://dx.doi.org/10.1016/j.pnsc.2018.11.002>.
- [17] L. Fan, Z. Tu, S.H. Chan, Recent development of hydrogen and fuel cell technologies: A review, Energy Rep. 7 (2021) 8421–8446, <http://dx.doi.org/10.1016/j.egyr.2021.08.003>.
- [18] D. Jafari, W.W. Wits, The utilization of selective laser melting technology on heat transfer devices for thermal energy conversion applications: A review, Renew. Sustain. Energy Rev. 91 (2018) 420–442, <http://dx.doi.org/10.1016/j.rser.2018.03.109>.
- [19] I. Kaur, P. Singh, State-of-the-art in heat exchanger additive manufacturing, Int. J. Heat Mass Transfer 178 (2021) 121600, <http://dx.doi.org/10.1016/j.ijheatmasstransfer.2021.121600>.
- [20] F. Careri, R.H.U. Khan, C. Todd, M.M. Attallah, Additive manufacturing of heat exchangers in aerospace applications: A review, Appl. Therm. Eng. 235 (2023) 121387, <http://dx.doi.org/10.1016/j.applthermaleng.2023.121387>.
- [21] M. Khaled, K. Faraj, H.E. Hage, J. Faraj, R. Taher, M. Mortazavi, Multi-passage concept applied to water-air cross flow tubes-and-fins heat exchangers – Thermal modelling and feasibility study, Int. J. Thermofluids 17 (2023) 100291, <http://dx.doi.org/10.1016/j.ijft.2023.100291>.
- [22] B. Torregrosa-Jaime, J.M. Corberán, J. Payá, J.L. Delamarche, Thermal characterisation of compact heat exchangers for air heating and cooling in electric vehicles, Appl. Therm. Eng. 115 (2017) 774–781, <http://dx.doi.org/10.1016/j.applthermaleng.2017.01.017>.
- [23] F.P. Incropera, D.P. DeWitt, T.L. Bergman, A.S. Lavine, Fundamentals of Heat and Mass Transfer, eighth ed., John Wiley & Sons, Hoboken, NJ, ISBN: 978-1-119-32042-5, 2017.
- [24] C.R. Ruivo, F. Dominguez-Muñoz, J.J. Costa, Simplified model of finned-tube heat exchangers based on the effectiveness method and calibrated with manufacturer and experimental data, Appl. Therm. Eng. 111 (2017) 340–352, <http://dx.doi.org/10.1016/j.applthermaleng.2016.09.115>.
- [25] M.-H. Kim, C.W. Bullard, Air-side performance of brazed aluminum heat exchangers under dehumidifying conditions, Int. J. Refrig. 25 (7) (2002) 924–934, [http://dx.doi.org/10.1016/S0140-7007\(01\)00106-2](http://dx.doi.org/10.1016/S0140-7007(01)00106-2).
- [26] T.C. Scott, D.S. Joshi, Engine cooling module sizing using combined 1-dimensional and CFD modeling tools, SAE Int. J. Passeng. Cars Mech. Syst. 2 (1) (2009) 1079–1098, <http://dx.doi.org/10.4271/2009-01-1177>.
- [27] T. Pujol, I. T'Jollyn, E. Massaguer, A. Massaguer, I.R. Cózar, M. De Paepe, Design optimization of plate-fin heat sink with forced convection for single-module thermoelectric generator, Appl. Therm. Eng. 221 (2023) 119866, <http://dx.doi.org/10.1016/j.applthermaleng.2022.119866>.
- [28] M.B. Kleiner, S.A. Kuehn, K. Habeger, High performance air cooling scheme using ducted microchannel parallel plate-fin heat sinks, in: Proceedings of 1995

- IEEE/CPMT 11th Semiconductor Thermal Measurement and Management Symposium, SEMI-THERM, 1995, pp. 122–130, <http://dx.doi.org/10.1109/STHERM.1995.512061>.
- [29] E. Rasouli, E. Fricke, V. Narayanan, High efficiency 3-D printed microchannel polymer heat exchangers for air conditioning applications, *Sci. Technol. Built Env.* 28 (3) (2022) 289–306, <http://dx.doi.org/10.1080/23744731.2022.2026693>.
- [30] R.P.P. da Silva, M.V.V. Morteau, K.V. de Paiva, L.E. Beckedorff, J.L.G. Oliveira, F.G. Brandão, A.S. Monteiro, C.S. Carvalho, H.R. Oliveira, D.G. Borges, V.L. Chastinet, Thermal and hydrodynamic analysis of a compact heat exchanger produced by additive manufacturing, *Appl. Therm. Eng.* 193 (2021) 116973, <http://dx.doi.org/10.1016/j.applthermaleng.2021.116973>.
- [31] R.K. Shah, D.P. Sekulić, *Fundamentals of Heat Exchanger Design*, John Wiley & Sons, Hoboken, NJ, ISBN: 978-0-471-32171-2, 2003.
- [32] H. Lim, U. Han, H. Lee, Design optimization of bare tube heat exchanger for the application to mobile air conditioning systems, *Appl. Therm. Eng.* 165 (2020) 114609, <http://dx.doi.org/10.1016/j.applthermaleng.2019.114609>.
- [33] M.A. Arie, A.H. Shoostari, V.V. Rao, S.V. Dessiatoun, M.M. Ohadi, Air-side heat transfer enhancement utilizing design optimization and an additive manufacturing technique, *J. Heat Transf.* 139 (3) (2016) 031901, <http://dx.doi.org/10.1115/1.4035068>.
- [34] R. Nacke, B. Northcutt, I. Mudawar, Theory and experimental validation of cross-flow micro-channel heat exchanger module with reference to high mach aircraft gas turbine engines, *Int. J. Heat Mass Transfer* 54 (5) (2011) 1224–1235, <http://dx.doi.org/10.1016/j.ijheatmasstransfer.2010.10.028>.
- [35] B. Northcutt, I. Mudawar, Enhanced design of cross-flow microchannel heat exchanger module for high-performance aircraft gas turbine engines, *J. Heat Transf.* 134 (6) (2012) 061801, <http://dx.doi.org/10.1115/1.4006037>.
- [36] D. Zhuang, Y. Yang, G. Ding, X. Du, Z. Hu, Optimization of microchannel heat sink with rhombus fractal-like units for electronic chip cooling, *Int. J. Refrig.* 116 (2020) 108–118, <http://dx.doi.org/10.1016/j.ijrefrig.2020.03.026>.
- [37] G. Nellis, S. Klein, *Heat Transfer*, Cambridge University Press, Cambridge, ISBN: 9780521881074, 2008.
- [38] M. Petrovic, K. Fukui, K. Kominami, Numerical and experimental performance investigation of a heat exchanger designed using topologically optimized fins, *Appl. Therm. Eng.* 218 (2023) 119232, <http://dx.doi.org/10.1016/j.applthermaleng.2022.119232>.
- [39] B.J. Hathaway, K. Garde, S.C. Mantell, J.H. Davidson, Design and characterization of an additive manufactured hydraulic oil cooler, *Int. J. Heat Mass Transfer* 117 (2018) 188–200, <http://dx.doi.org/10.1016/j.ijheatmasstransfer.2017.10.013>.
- [40] A.J. Modi, M.K. Rathod, Characterization of thermal and hydraulic performance of fin-and-tube heat exchanger using rectangular winglet vortex generator with punched hole, in: WCX SAE World Congr. Exp, SAE International, 2020, <http://dx.doi.org/10.4271/2020-01-1346>.
- [41] Y.-T. Lee, L.-H. Chien, J. He, C.-Y. Wen, A.-S. Yang, Air side performance characterization of wavy Fin-and-tube heat exchangers having elliptic tubes with large waffle heights, *Appl. Therm. Eng.* 217 (2022) 119220, <http://dx.doi.org/10.1016/j.applthermaleng.2022.119220>.
- [42] F. Feppon, G. Allaire, C. Dapogny, P. Jolivet, Body-fitted topology optimization of 2D and 3D fluid-to-fluid heat exchangers, *Comput. Methods Appl. Mech. Engrg.* 376 (2021) 113638, <http://dx.doi.org/10.1016/j.cma.2020.113638>.
- [43] S.H. Oh, J.E. Kim, C.H. Jang, et al., Multifunctional gradations of TPMS architected heat exchanger for enhancements in flow and heat exchange performances, *Sci. Rep.* 15 (2025) 19931, <http://dx.doi.org/10.1038/s41598-025-04940-2>, (Accessed 8 August 2025).
- [44] T. Si, K. Sun, H. Zhang, Q. Wang, Z. Cheng, Lattice-scale topology optimization of TPMS structure for heat transfer, *Int. J. Heat Mass Transfer* 251 (2025) 127288, <http://dx.doi.org/10.1016/j.ijheatmasstransfer.2025.127288>.
- [45] F. Beltrame, P. Colonna, C.M. De Servi, Optimal design of aircraft thermal systems and their heat exchangers leveraging a data-driven surrogate model, *Int. J. Heat Mass Transfer* 253 (2025) 127502, <http://dx.doi.org/10.1016/j.ijheatmasstransfer.2025.127502>.
- [46] S. Mohapatra, D.K. Das, A.K. Singh, Plate-fin heat exchanger optimal design for industry using both single and multi-objective granularity based surrogate assisted kho-kho optimization, *Ann. Nucl. Energy* 223 (2025) 111605, <http://dx.doi.org/10.1016/j.anucene.2025.111605>.
- [47] H.R. Abbasi, E. Sharifi Sedeh, H. Pourrahmani, M.H. Mohammadi, Shape optimization of segmental porous baffles for enhanced thermo-hydraulic performance of shell-and-tube heat exchanger, *Appl. Therm. Eng.* 180 (2020) 115835, <http://dx.doi.org/10.1016/j.applthermaleng.2020.115835>.
- [48] S.K. Sarangi, D.P. Mishra, H. Ramachandran, N. Anand, V. Masih, L.S. Brar, Analysis and optimization of the curved trapezoidal winglet geometry in a high-efficiency compact heat exchanger, *Int. J. Therm. Sci.* 164 (2021) 106872, <http://dx.doi.org/10.1016/j.ijthermalsci.2021.106872>.
- [49] J.L. Mason, Heat transfer in crossflow, in: *Proceedings of Second US National Congress of Applied Mechanics*, Ann Arbor, MI, USA, 1954, pp. 801–803.
- [50] R.L. Panton, *Incompressible flow*, in: *Incompressible Flow*, John Wiley & Sons, Hoboken, NJ, ISBN: 9781118713075, 2013, pp. 198–219, <http://dx.doi.org/10.1002/9781118713075.ch10>.
- [51] W.M. Kays, A.L. London, *Compact Heat Exchangers*, third ed., Krieger Publishing Company, Malabar, FL, ISBN: 978-1575240602, 1998.
- [52] S.W. Churchill, Friction-factor equation spans all fluid-flow regimes, *Chem. Eng.* 84 (24) (1977) 91–92.
- [53] P. Gradl, A. Cervone, P. Colonna, Enhancement of friction factors for microchannels fabricated using laser powder directed energy deposition, *Mater. Des.* 251 (2025) 113673, <http://dx.doi.org/10.1016/j.matdes.2025.113673>.
- [54] M. Kadivar, D. Tormey, G. McGranaghan, A review on turbulent flow over rough surfaces: Fundamentals and theories, *Int. J. Thermofluids* 10 (2021) 100077, <http://dx.doi.org/10.1016/j.ijft.2021.100077>.
- [55] I.H. Bell, J. Wronski, S. Quoilin, V. Lemort, Pure and pseudo-pure fluid thermophysical property evaluation and the open-source thermophysical property library CoolProp, *Ind. Eng. Chem. Res.* 53 (6) (2014) 2498–2508, <http://dx.doi.org/10.1021/ie4033999>.
- [56] M.V.V. Morteau, L.H.R. Cisterna, K.V. Paiva, M.B.H. Mantelli, Thermal and hydrodynamic analysis of a cross-flow compact heat exchanger, *Appl. Therm. Eng.* 150 (2019) 750–761, <http://dx.doi.org/10.1016/j.applthermaleng.2019.01.038>.
- [57] L. Luo, Z. Fan, H. Le Gall, X. Zhou, W. Yuan, Experimental study of constructal distributor for flow equidistribution in a mini crossflow heat exchanger (MCHE), *Chem. Eng. Process.: Process. Intensif.* 47 (2) (2008) 229–236, <http://dx.doi.org/10.1016/j.ccep.2007.02.028>.
- [58] L.L. Hein, M.V.V. Morteau, Theoretical and experimental thermal performance analysis of an additively manufactured polymer compact heat exchanger, *Int. Commun. Heat Mass Transf.* 124 (2021) 105237, <http://dx.doi.org/10.1016/j.icheatmasstransfer.2021.105237>.
- [59] EOS GmbH – Electro Optical Systems, PA 2200 product information: Thermal conductivity of sintered parts, 2025, https://www.epmi-impression-3d.com/pdf/EOS_PA12.pdf. Thermal conductivity vertical to sintered layers: 0.144 W/(m · K), parallel to sintered layers: 0.127 W/(m · K), measured per DIN 52616. Accessed 8 September 2025.
- [60] R.P.P. da Silva, M.V.V. Morteau, F.J. dos Santos, G. Zilio, K.V. de Paiva, J.L.G. Oliveira, Discretized and experimental investigation of thermo-hydraulic behavior in a compact heat exchanger manufactured via SLM process, *Therm. Sci. Eng. Prog.* 46 (2023) 102184, <http://dx.doi.org/10.1016/j.tsep.2023.102184>.
- [61] K. Kempen, F. Welkenhuyzen, J. Qian, J.-P. Kruth, Dimensional accuracy of internal channels in SLM produced parts, in: *Proceedings of the ASPE 2014 Spring Topical Meeting: Dimensional Accuracy and Surface Finish in Additive Manufacturing*, American Society for Precision Engineering, San Francisco, USA, ISBN: 9781887706643, 2014, pp. 76–79.
- [62] G.F. Nellis, S.A. Klein, *Numerical modeling of cross-flow heat exchangers*, in: *Heat Transfer*, Cambridge University Press, ISBN: 9780521881074, 2008, pp. 919–937.
- [63] J.E. Hesselgreaves, R. Law, D. Reay, *Compact Heat Exchangers: Selection, Design and Operation*, second ed., Butterworth-Heinemann, Oxford, ISBN: 978-0-08-100305-3, 2016.
- [64] R.K. Shah, A.L. London, *Laminar Flow Forced Convection in Ducts: A Source Book for Compact Heat Exchanger Analytical Data*, first ed., Academic Press, New York, ISBN: 0-12-020051-1, 1978.
- [65] V. Gnielinski, G1 heat transfer in pipe flow, in: *VDI Heat Atlas*, Springer Berlin Heidelberg, Berlin, Heidelberg, ISBN: 978-3-540-77877-6, 2010, pp. 691–700, http://dx.doi.org/10.1007/978-3-540-77877-6_34.
- [66] M.V.V. Morteau, M.B.H. Mantelli, Nusselt number correlation for compact heat exchangers in transition regimes, *Appl. Therm. Eng.* 151 (2019) 514–522, <http://dx.doi.org/10.1016/j.applthermaleng.2019.02.017>.
- [67] V. Gnielinski, Neue gleichungen für den wärme- und den stoffübergang in turbulent durchströmten rohren und kanälen, *Forsch. Ingenieurwesen A* 41 (1) (1975) 8–16, <http://dx.doi.org/10.1007/BF02559682>.
- [68] V. Gnielinski, On heat transfer in tubes, *Int. J. Heat Mass Transfer* 63 (2013) 134–140, <http://dx.doi.org/10.1016/j.ijheatmasstransfer.2013.04.015>.
- [69] H. Schlichting, *Boundary Layer Theory*, Seventh ed., McGraw-Hill Classic Textbook Reissue Series, McGraw-Hill, New York, ISBN: 9780070553347, 1979.
- [70] R.K. Shah, A correlation for laminar hydrodynamic entry length solutions for circular and noncircular ducts, *J. Fluids Eng.* 100 (2) (1978) 177–179, <http://dx.doi.org/10.1115/1.3448626>.
- [71] Z. qing Wang, Study on correction coefficients of laminar and turbulent entrance region effect in round pipe, *Appl. Math. Mech.* 3 (3) (1982) 433–446, <http://dx.doi.org/10.1007/BF01897224>.
- [72] P.-S. Lee, S.V. Garimella, Thermally developing flow and heat transfer in rectangular microchannels of different aspect ratios, *Int. J. Heat Mass Transfer* 49 (17) (2006) 3060–3067, <http://dx.doi.org/10.1016/j.ijheatmasstransfer.2006.02.011>.
- [73] I.E. Idelchik, *Handbook of Hydraulic Resistance*, fourth ed., Begell House, New York, ISBN: 978-1-56700-251-5, 2007, Revised and augmented edition.
- [74] Y.A. Çengel, J.M. Cimbala, *Fluid Mechanics: Fundamentals and Applications*, third ed., McGraw-Hill Education, New York, ISBN: 978-0-07-338032-2, 2013.